We are IntechOpen, the world's leading publisher of Open Access books Built by scientists, for scientists

4,800
Open access books available

122,000
International authors and editors

135M
Downloads

Our authors are among the

154
Countries delivered to

TOP 1%
most cited scientists

12.2%
Contributors from top 500 universities

WEB OF SCIENCE™

Selection of our books indexed in the Book Citation Index in Web of Science™ Core Collection (BKCI)

Interested in publishing with us?
Contact book.department@intechopen.com

Numbers displayed above are based on latest data collected.
For more information visit www.intechopen.com

6

Acoustic Waves in Phononic Crystal Plates

Xin-Ye Zou, Xue-Feng Zhu, Bin Liang and Jian-Chun Cheng
Nanjing University,
People's Republic of China

1. Introduction

Recently, the study on elastic waves in phononic crystal plates is becoming a research hotspot due to its potential applications, especially in wireless communication, transducer and sensor system [1-10]. The phononic crystal plates commonly consist of two materials with large contrast in elastic properties and densities, arranging in a periodic (or quasiperiodic) array. The absolute band gaps in composite plates can forbid the propagation of all elastic wave modes in all directions. Comparing with the bulk wave and surface acoustic wave devices, phononic crystal plates have better performance in elastic wave propagation since the phase speed of most Lamb wave modes (except for A_0 mode) is faster than surface wave mode, and also the wave energy in plates is totally confined between the upper and nether free-stress boundaries regardless of the air damp and self-dissipation, which provides a special potentiality in micro-electronics in wireless communication.

The propagation of Lamb waves is much more complicated than bulk wave and surface acoustic wave in terms of the free-stress boundaries which can couple the longitudinal and transversal strain components. The first attempt to describe the propagation of Lamb waves with wavelength comparable with the lattice is due to Auld and co-workers [11-12], who studied 2D composites within the couple-mode approximation. Alippi et al. [13] have presented an experimental study on the stopband phenomenon of lowest-order Lamb waves in piezoelectric periodic composite plates and interpreted their results in terms of a theoretical model, which provides approximate dispersion curves of the lowest Lamb waves in the frequency range below the first thickness mode by assuming no coupling between different Lamb modes. The transmissivity of the finite structure to Lamb wave modes was also calculated by taking into account the effective plate velocities of the two constituent materials [14]. Based on a rigorous theory of elastic wave, Chen et al.[1] have employed plane wave expansion (PWE) method and transient response analysis (TRA) to demonstrate the existence of stop bands for lower-order Lamb wave modes in 1D plate. Gao et al.[8] have developed a virtual plane wave expansion (V-PWE) method to study the substrate effect on the band gaps of lower-order Lamb waves propagating in thin plate with 1D phononic crystal coated on uniform substrate. They also studied the quasiperiodic (Fibonacci system) 1D system and find out the existence of split in phonon band gap [2]. In order to reduce the computational complexity without losing the accuracy, Zhu et al.[9] have promoted an efficient method named harmony response analysis (HRA) and supercell plane wave expansion (SC PWE) to study the behavior of Lamb wave in silicon-based 1D composite plates. Zou et al.[10] have employed V-PWE method to study the band gaps of plate-mode waves in 1D piezoelectric composite plates with substrates.

Source: Acoustic Waves, Book edited by: Don W. Dissanayake,
ISBN 978-953-307-111-4, pp. 466, September 2010, Sciyo, Croatia, downloaded from SCIYO.COM

The chapter is structured as follows: we firstly introduce the theory and modeling used in this chapter in Section 2. In Section 3, we focus on the band gaps of lower-order Lamb waves in 1D composite thin plates without/with substrate. In Section 4, we study the lamb waves in 1D quasiperiodic composite thin plates. In Section 5, we focus on acoustic wave behavior in silicon-based 1D phononic crystal plates for different structures, and finally in Section 6, we study the band gaps of plate-mode waves in 1D piezoelectric composite plates without/with substrates.

2. Theory and modeling of phononic crystal plates

In this section, we give the theory and modeling of phononic crystal plates with different structures: the periodic structure without/with substrate, and the quasiperiodic structure.

2.1 Periodic structure without substrate by PWE method

As shown in Fig. 1, the periodic composite plate consists of material A with width d_{A}, material B with d_{B}, lattice spacing $D = d_{\mathrm{A}} + d_{\mathrm{B}}$, and filling rate defined by $f = d_{\mathrm{A}} / D$. The wave propagates along the x direction of a plate bounded by planes $z = 0$ and $z = L$.

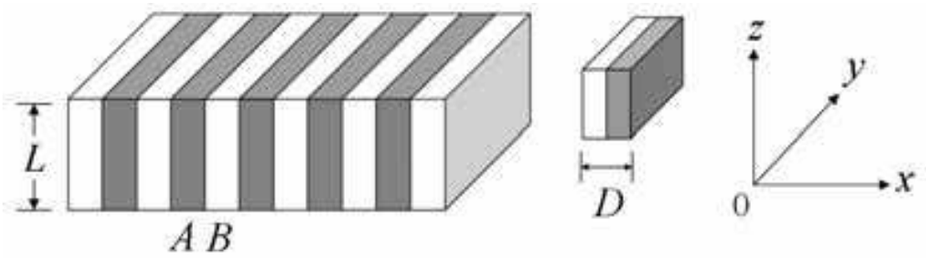

Fig. 1. 1D periodic composite plate consisting of alternate A and B strips.

In the periodic structure, all field components are assumed to be independent of the y direction. In an inhomogeneous linear elastic medium with no body force, the equation of motion for displacement vector $\boldsymbol{u}(x,z,t)$ can be written as

$$\rho(x)\ddot{\boldsymbol{u}}_p = \partial_q[c_{pqmn}(x)\partial_n \boldsymbol{u}_m], \quad (p = 1,2,3), \tag{1}$$

where $\rho(x)$ and $c_{pqmn}(x)$ are the x-dependent mass density and elastic stiffness tensor, respectively. Due to the spatial periodicity in the x direction, the material constants, $\rho(x)$ and $c_{pqmn}(x)$ can be expanded in the Fourier series with respect to the 1D reciprocal lattice vectors (RLVs), as follows

$$\rho(x) = \sum_G e^{jGx}\rho_G, \tag{2}$$

$$c_{pqmn}(x) = \sum_G e^{jGx}c^G_{pqmn}, \tag{3}$$

where ρ_G and c^G_{pqmn} are expansion coefficients of the mass density and elastic stiffness tensor, respectively. From the Bloch theorem and by expanding the displacement vector $\boldsymbol{u}(x,z,t)$ into Fourier series, one obtains

$$\boldsymbol{u}(x,z,t) = \sum_{G} e^{jk_x x - j\omega t}(e^{jGx}\boldsymbol{A}_G e^{jk_z z}), \tag{4}$$

where k_x is a Bloch wave vector and ω is the circular frequency, $\boldsymbol{A}_G = (A_G^1, A_G^2, A_G^3)$ is the amplitude vector of the partial waves, and k_z is the wave number of the partial waves along the z direction. Substituting Eqs. (2)-(4) into Eq. (1), one obtains homogenous linear equations to determine both (A_G^1, A_G^2, A_G^3) and k_z.

$$\begin{pmatrix} c_{11}(k_x+G)(k_x+G') + c_{44}k_z^2 - \rho\omega^2 & 0 & c_{12}(k_x+G) + c_{44}(k_x+G')k_z \\ 0 & c_{44}(k_x+G)(k_x+G') + c_{44}k_z^2 - \rho\omega^2 & 0 \\ c_{12}(k_x+G') + c_{44}(k_x+G)k_z & 0 & c_{44}(k_x+G)(k_x+G') + c_{11}k_z^2 - \rho\omega^2 \end{pmatrix} \begin{pmatrix} A_{G'}^1 \\ A_{G'}^2 \\ A_{G'}^3 \end{pmatrix} = 0, \tag{5}$$

Supposing that the materials A and B are cubic materials, it is obvious that the wave motion polarized in the y-direction, namely SH wave, decouples to the wave motions polarized in the x- and z-directions, namely, P and SV waves. It is relatively simple to discuss the SH wave so that we focus our attentions to P and SV waves, and the equation of motion for Lamb waves becomes

$$\begin{pmatrix} c_{11}(k_x+G)(k_x+G') + c_{44}k_z^2 - \rho\omega^2 & c_{12}(k_x+G) + c_{44}(k_x+G')k_z \\ c_{12}(k_x+G') + c_{44}(k_x+G)k_z & c_{44}(k_x+G)(k_x+G') + c_{11}k_z^2 - \rho\omega^2 \end{pmatrix} \begin{pmatrix} A_{G'}^1 \\ A_{G'}^3 \end{pmatrix} = 0, \tag{6}$$

If one truncates the expansions of Eqs. (2) and (3) by choosing n RLVs, one will obtain $4n$ eigenvalues $k_z^{(l)}$, $(l = 1-4n)$. For the Lamb waves, all of the $4n$ eigenvalues $k_z^{(l)}$ must be included. Accordingly, displacement vector of the Lamb waves can be taken of the form

$$\boldsymbol{u}(x,z,t) = \sum_{G}{}' e^{i(k_x+G)x - i\omega t}\left(\sum_{l=1}^{4n} \boldsymbol{A}_G e^{iK_z^{(l)}z}\right) = \sum_{G}{}' e^{i(k_x+G)x - i\omega t}\left(\sum_{l=1}^{4n} X_l \varepsilon_G^{(l)} e^{ik_z^{(l)}z}\right), \tag{7}$$

where $\varepsilon_G^{(l)}$ is the associated eigenvector for the eigenvalue $k_z^{(l)}$, X_l is the weighting coefficient to be determined, and the prime of the summation expresses that the sum over G is truncated up to n.

The boundary conditions are the stress-free on the upper (z = 0) and rear ($z = L$) surfaces

$$\boldsymbol{T}_{p3}\big|_{z=0,L} = c_{p3mn}\partial_n u_m\big|_{z=0,L} = 0 \qquad (p = 1,3). \tag{8}$$

which $\boldsymbol{T}_{p3}$ is the stress tensor and L is the plate thickness. Eq. (8) leads to $4n$ homogeneous linear equations for X_l l = (1- $4n$), as follows

$$\begin{bmatrix} H_{1,G}^{(1)} & H_{1,G}^{(2)} & \cdots & H_{1,G}^{(4n)} \\ H_{2,G}^{(1)} & H_{2,G}^{(2)} & \cdots & H_{2,G}^{(4n)} \\ H_{3,G}^{(1)} & H_{3,G}^{(2)} & \cdots & H_{3,G}^{(4n)} \\ H_{4,G}^{(1)} & H_{4,G}^{(2)} & \cdots & H_{4,G}^{(4n)} \end{bmatrix} \begin{bmatrix} X_1 \\ X_2 \\ \vdots \\ X_{4n} \end{bmatrix} = \tilde{H}X = 0, \tag{9}$$

where $\tilde{H}$ is a $4n \times 4n$ matrix with components

$$H_{1,G}^{(l)} = C_{G-G'}^{44}[(k_x + G')\varepsilon_{G'}^{3(l)} + k_z^{(l)}\varepsilon_{G'}^{1(l)}], \tag{10a}$$

$$H_{2,G}^{(l)} = C_{G-G'}^{11}k_z^{(l)}\varepsilon_{G'}^{3(l)} + C_{G-G'}^{12}(k_x + G')\varepsilon_{G'}^{1(l)}, \tag{10b}$$

$$H_{3,G}^{(l)} = C_{G-G'}^{44}[(k_x + G')\varepsilon_{G'}^{3(l)} + k_z^{(l)}\varepsilon_{G'}^{1(l)}] \times \exp(jk_z^{(l)}L), \tag{10c}$$

$$H_{4,G}^{(l)} = [C_{G-G'}^{11}k_z^{(l)}\varepsilon_{G'}^{3(l)} + C_{G-G'}^{12}(k_x + G')\varepsilon_{G'}^{1(l)}] \times \exp(jk_z^{(l)}L). \tag{10d}$$

From Eq. (9) one notes that to obtain nontrivial solution for the X_l, the determinant of the boundary condition matrix should be equal to zero. The ω of the Lamb wave modes are thus found by searching for the values of ω that simultaneously make the Eq. (6) and $\det(\tilde{H})$ equal to zero. In practice, an iterative search procedure is usually required to find these ω [15-16].

2.2 Periodic structure with substrate by V-PWE method

As shown in Fig.2, the composite plate with substrate consists of the 1D phononic crystal (PC) layer coated on C substrate. The PC layer consists of the material A with the width d_A and the material B with the width d_B.

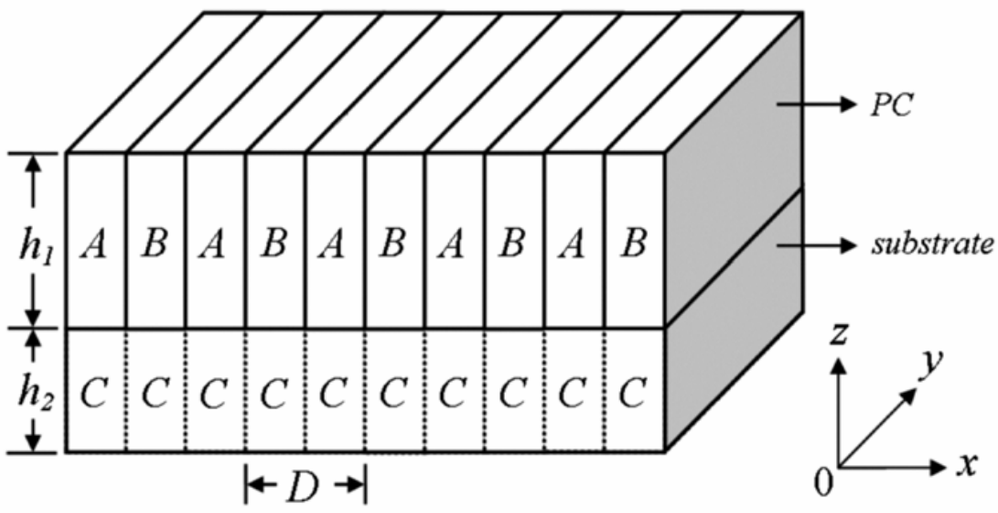

Fig. 2. The 1D periodic composite plate consisting of alternate A and B strips with a substrate C.

We develop a V-PWE method to calculate the dispersion curves of Lamb wave modes propagating along the x direction in the presence of the uniform substrate. Here, we give the equations of V-PWE method for the piezoelectric periodic structure with substrate. One can have the equations for non-piezoelectric situation by omitting the piezoelectricity components and the electrical boundary conditions.

In the situation of piezoelectric composite plate with substrate, the equations governing the motion of lattice displacement $\boldsymbol{u}^m(x,z,t)$ and electrical displacement $\boldsymbol{D}^m(x,z,t)$ in this inhomogeneous system are given by

$$\rho^m(x)\ddot{u}_j^m = \partial_i T_{ij}^m, \tag{11}$$

$$\partial_i D_i^m = 0, \tag{12}$$

$$T_{ij}^m = c_{ijkl}^m(x)\partial_l u_k^m + e_{lij}^m(x)\partial_l \phi^m, \tag{13}$$

$$D_i^m = e_{ikl}^m(x)\partial_l u_k^m - \varepsilon_{il}^m(x)\partial_l \phi^m, \tag{14}$$

where $i,j,k,l = x,z$; $m = 1,2$ (1 represents phononic layer; 2 represents the substrate, respectively). $\boldsymbol{T}_{ij}^m(x,z,t)$, $\boldsymbol{D}^m(x,z,t)$, $\boldsymbol{u}^m(x,z,t)$, $\varphi^m(x,z,t)$, $\rho^m(x)$, $c_{ijkl}^m(x)$, $e_{lij}^m(x)$, and $\varepsilon_{il}^m(x)$ are the stress vector, electrical displacement vector, displacement vector, electric potential, x-dependent mass density, elastic stiffness, piezoelectric, and dielectric constant tensors, respectively. It comes into notice that in fact the material constants depend on the z-direction due to the existence of the substrate, as follows

$$\alpha(x,z) = \begin{cases} \alpha^1(x), & (0 < z < h_1) \\ \alpha^2, & (-h_2 < z < 0) \end{cases} \tag{15}$$

where $\alpha = (\rho, c_{ijkl}, e_{lij}, \varepsilon_{il})$, $(\rho^2, c_{ijkl}^2, e_{lij}^2, \varepsilon_{il}^2)$ are the material constants for the substrate.

Due to the spatial periodicity, the Bloch theorem can be applied to the PC layer, but it cannot be simply applied to the substrate layer. However, one notice that the triangle basic function set in the Fourier series is an orthogonal and complete set, each components in the Fourier series must satisfied the boundary conditions at the interface between the PC layer and the substrate at z = 0, namely the continuities of the normal stress, normal displacement, normal electrical displacement and electric potential.

$$T_{iz}^1\Big|_{z=0} = T_{iz}^2\Big|_{z=0},\ u_{iz}^1\Big|_{z=0} = u_{iz}^2\Big|_{z=0},\ D_z^1\Big|_{z=0} = D_z^2\Big|_{z=0},\ \phi^1\Big|_{z=0} = \phi^2\Big|_{z=0},\ (i = x,z). \tag{16}$$

Therefore, the displacement and electric potential fields in the substrate layer also must be expanded to the Fourier series with the period that is same as the PC layer in order to satisfy the boundary conditions. Then the substrate layer can be treated as a virtual periodic structure that has the same filling fraction and period as the PC layer. Thereupon, the Bloch theorem can be applied to both the PC and the substrate layers.

Due to the spatial periodicity in the x direction, the material constants can be expanded in Fourier series with respect to the 1-D reciprocal-lattice vector (RLV) G, as follows:

$$\alpha(x) = \sum_G e^{jGx}\alpha_G, \tag{17}$$

where α_G is the corresponding Fourier coefficient. Utilizing the Bloch theorem and expanding the displacement vector and electric potential into Fourier series in the PC and the substrate layers, one obtains

$$\boldsymbol{u}^m(x,z,t)=\sum_G e^{j(k_x x-\omega t)}(e^{jGx}\mathrm{A}_G^m e^{jk_z^m z}), \tag{18}$$

$$\phi^m(x,z,t)=\sum_G e^{j(k_x x-\omega t)}(e^{jGx}A_{G3}^m e^{jk_z^m z}), \tag{19}$$

where k_x is a Bloch wave vector, ω is the circular frequency, and k_z^m is the wave number along the z-direction, $\boldsymbol{A}_G^m=(A_{G1}^m,A_{G2}^m)$ and A_{G3}^m are the amplitude vectors of the partial waves and electric potential, respectively. Substituting Eqs. (17)-(19) into Eqs. (11)-(14), one can obtain the eigenvalue problem with respect to k_z^m:

$$(\boldsymbol{A}^m k_z^{m2}+\boldsymbol{B}^m k_z^m+\boldsymbol{C}^m)\cdot \mathrm{U}^m=0, \tag{20}$$

where $\boldsymbol{U}^m=\{A_{G1}^m,A_{G2}^m,A_{G3}^m\}^T$ is called the generalized displacement vector, the $3n\times 3n$ matrices $\boldsymbol{A}^m$, $\boldsymbol{B}^m$, and $\boldsymbol{C}^m$ are functions of k_x, G, ω, ρ_G^m, $c_G^{ijkl m}$, e_G^{lijm}, ε_G^{ilm}, and n is the number of RLV.

Here, we consider the stress-free boundary conditions and two kinds of the electrical boundary conditions. For the 1-D problem, we have

the stress free boundary conditions:

$$T_{iz}^1\Big|_{z=h_1}=0,\quad T_{iz}^2\Big|_{z=-h_2}=0,\ \ (i=x,z), \tag{21}$$

the OC boundary conditions:

$$D_z^1\Big|_{z=h_1}=D_z^{air}\Big|_{z=h_1},\quad \phi^1\Big|_{z=h_1}=\phi^{air}\Big|_{z=h_1},$$

$$D_z^2\Big|_{z=-h_2}=D_z^{air}\Big|_{z=-h_2},\ \phi^2\Big|_{z=-h_2}=\phi^{air}\Big|_{z=-h_2}, \tag{22}$$

$$(D_z^{air}=-\varepsilon_0\frac{\partial\phi^{air}}{\partial z},\quad \varepsilon_0=1\times 10^{-11}\mathrm{F/m},)$$

the SC boundary conditions:

$$\phi^1\Big|_{z=h_1}=0,\qquad \phi^2\Big|_{z=-h_2}=0. \tag{23}$$

Putting $A_G^{j(l)m}=X_l^m\beta_G^{j(l)m}$ ($j=1-3$, $l=1-6n$, $m=1,2$), where $\beta_G^{j(l)m}$ is the associated eigenvector of the eigenvalue $k_z^{(l)m}$, and X_l^m is the weighting coefficient that can be determined from the boundary conditions for different layers, one obtains: $\mathbf{H}\cdot\mathbf{X}=0$ from the equations (16), (21) and (22) [or (23)], where $\mathbf{H}$ is a $12n\times 12n$ matrix. The existence of a nontrivial solution of X_l^m needs the determinant of matrix $\mathbf{H}$ to be zero

$$\det(\mathbf{H})=0. \tag{24}$$

Then one can obtain the dispersion relations of the Lamb waves propagating in a 1-D PC layer coated on a substrate.

2.3 Periodic structure without/with substrate by FE method

In order to study the elastic wave in the phononic crystal plates, transient response analysis (TRA) and the harmony response analysis (HRA) are presented here by finite element (FE) method.

First, the TRA is employed to calculate the transmitted power spectra (TPS) for the finite periodic structure. The FE solution involves the discretization of the domain into a number of elements, approximating the displacement values interior to the elements in term of its nodal value through the shape functions of the chosen element and the determination of nodal values [17].

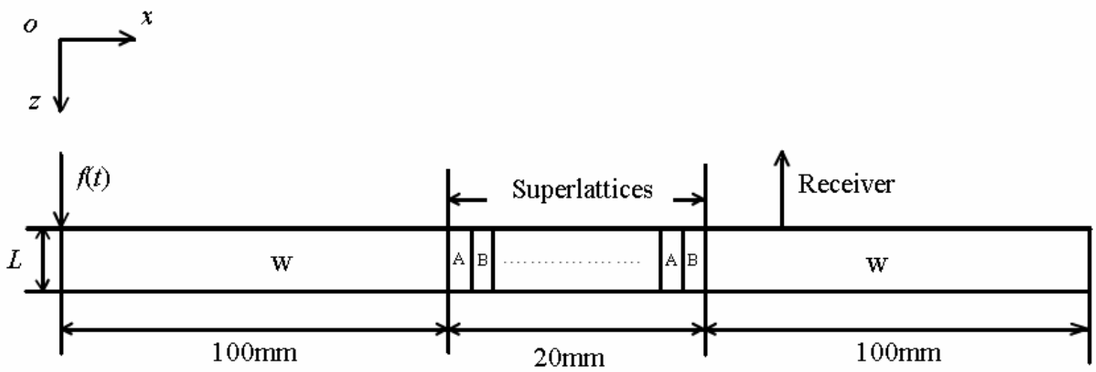

Fig. 3. Modified plate geometry in the Finite Element calculations

Fig. 3 shows the configuration of the modified composite plate in the Finite Element calculations, in which the superlattices with ten periods (the length is 20 mm) is bounded by two pure tungsten plates (the length is 100 mm) at two sides. Lamb waves are excited by the force function $f(t)$ that is a triangle wave at $x = 0$, and are received at $x = 140$ mm [18]. The generation source is far from the periodic structure in order to obtain approximate plane waves when the wavefronts reach it. The step sizes of temporal and spatial discretization in the finite model are fine enough for the convergence of the numerical results (increasing the number of elements of the finite element mesh is equivalent to increasing the number of harmonics in PWE method). The vertical displacement of a node at upper surface of the plate behind the superlattices array at $x = 140$ mm is collected as function of time. For a sufficiently large number of these vertical displacement data on the time axis, the displacement fields are Fourier transformed into the frequency domain to yield the TPS.

We also promote an efficient method named HRA to study the propagation and transmission of acoustic waves in 1D phononic crystal plates. Comparing with TRA [1,2,8], HRA is more time-saving due to its direct calculation in frequency domain and more powerful for the acquirability of displacement field under certain frequency load, which can be further employed to the designation of various phononic crystal functionalities such as filters, resonators and waveguides. With this method, we can study the cases both without and with substrates. Taking the gradient of the displacement fields, we can further study the strain distribution in the plates, and it is really a very direct way to understand how the band gaps form in phononic crystal plates by comparing displacement fields under different frequency loads (inside/outside band gaps).

Any continual periodic loads can produce continual periodic response (harmony response) in phononic crystal plates. HRA is a method used to define the stabilized response of linear structures under time-harmonic loads. By calculating the responses (usually displacement fields) under different frequency loads, we can obtain the transmitted power spectra in the detected region. HRA is a linear analysis regardless of any nonlinear characteristics. For multi-element structure, the Newton's second law can be expressed as follows:

$$[\boldsymbol{M}]\{\ddot{\boldsymbol{D}}\}+[\boldsymbol{C}]\{\dot{\boldsymbol{D}}\}+\{\boldsymbol{R}^{int}\}=\{\boldsymbol{R}^{ext}\} \tag{25a}$$

$$\{\boldsymbol{R}^{int}\}=[\boldsymbol{K}]\{\boldsymbol{D}\} \tag{25b}$$

$$\{\boldsymbol{R}^{ext}\}=\{\boldsymbol{F}\}\exp(i\Omega t) \tag{25c}$$

where $[\boldsymbol{M}]$, $[\boldsymbol{C}]$ and $[\boldsymbol{K}]$ are general mass matrix, damping matrix and stiffness matrix, respectively; $\{\boldsymbol{D}\}$ and $\{\boldsymbol{F}\}\exp(i\Omega t)$ are nodal degree of freedom vector and nodal external load vector, respectively. Eq (25a) describes a dynamic balance among inertial force, damping force, inner force $\{\boldsymbol{R}^{int}\}$ and external load force $\{\boldsymbol{R}^{ext}\}$. The forced vibration of the structure will finally come to a stabilized status in which every node moves in harmonic motion with the same frequency (Ω). Further, we can express $\{\boldsymbol{D}\}$ into:

$$\{\boldsymbol{D}\}=\{\bar{\boldsymbol{D}}\}\exp(i\Omega t) \tag{26}$$

where $\{\bar{\boldsymbol{D}}\}$ is the complex nodal degree of freedom vector. By substituting Eq (26) into Eqs (25a)-(25c), we can obtain:

$$\left([\boldsymbol{K}]+i\Omega[\boldsymbol{C}]-\Omega^2[\boldsymbol{M}]\right)\{\bar{\boldsymbol{D}}\}=\{\boldsymbol{F}\} \tag{27}$$

where $\{\bar{\boldsymbol{D}}\}$ can be obtained using Frontal solver. We choose imaginary component of $\{\bar{\boldsymbol{D}}\}$ to build up the stabilized displacement field under different frequency loads. It is necessary to mention that TRA requires much more substeps to obtain the nodal degree of freedom vector at certain detected time for the reason that the time step Δt should obey the following criterion for numerical convergence in Newmark method: [19]

$$\Delta t \le \frac{\Omega_{crit}}{2\pi f_{max}} \tag{28}$$

where f_{max} is the maximum frequency of interest. Ω_{crit} is defined to be:

$$\Omega_{crit}=\left(\frac{\gamma}{2}-\beta\right)^2 \tag{29}$$

where β is chosen to be $(\gamma+1/2)^2/4$ with $\gamma \ge 1/2$ to achieve as large high frequency dissipation as possible. We choose $\beta=0.2756$, $\gamma=0.55$ in the numerical calculation of TRA. In each substep, a very complex iteration is employed, which takes the form:

$$\left[\boldsymbol{K}^{eff}\right]\left\{\boldsymbol{D}\right\}_{n+1}=\left\{\boldsymbol{R}^{ext}\right\}_{n+1}+\left[\boldsymbol{M}\right]\left(\frac{\left\{\boldsymbol{D}\right\}_{n+1}}{\beta\Delta t^{2}}+\frac{\left\{\dot{\boldsymbol{D}}\right\}_{n}}{\beta\Delta t}+\frac{\left\{\ddot{\boldsymbol{D}}\right\}_{n}\left(1-2\beta\right)}{2\beta}\right)$$
$$+\left[\boldsymbol{C}\right]\left(\frac{\left\{\boldsymbol{D}\right\}_{n}\gamma}{\beta\Delta t}+\frac{\left\{\dot{\boldsymbol{D}}\right\}_{n}\left(\gamma-\beta\right)}{\beta}+\frac{\left\{\ddot{\boldsymbol{D}}\right\}_{n}\Delta t\left(\gamma-2\beta\right)}{2\beta}\right) \tag{30a}$$

$$\left\{\dot{\boldsymbol{D}}\right\}_{n+1}=\frac{\left(\left\{\boldsymbol{D}\right\}_{n+1}-\left\{\boldsymbol{D}\right\}_{n}\right)\gamma}{\beta\Delta t}-\frac{\left\{\dot{\boldsymbol{D}}\right\}_{n}\left(\gamma-\beta\right)}{\beta}-\frac{\left\{\ddot{\boldsymbol{D}}\right\}_{n}\Delta t\left(\gamma-2\beta\right)}{2\beta} \tag{30b}$$

$$\left\{\ddot{\boldsymbol{D}}\right\}_{n+1}=\frac{\left(\left\{\boldsymbol{D}\right\}_{n+1}-\left\{\boldsymbol{D}\right\}_{n}-\Delta t\left\{\dot{\boldsymbol{D}}\right\}_{n}\right)}{\beta\Delta t^{2}}-\frac{\left\{\ddot{\boldsymbol{D}}\right\}_{n}\left(1-2\beta\right)}{2\beta} \tag{30c}$$

where $\left[\boldsymbol{K}^{eff}\right]=\left[\boldsymbol{M}\right]/\left(\beta\Delta t^{2}\right)+\left[\boldsymbol{C}\right]\gamma/\left(\beta\Delta t\right)+\left[\boldsymbol{K}\right]$. The initial condition for Eqs (30a)-(30c) is shown as follows:

$$\left\{\ddot{\boldsymbol{D}}\right\}_{0}=\left[\boldsymbol{M}\right]^{-1}\left(\left\{\boldsymbol{R}^{ext}\right\}_{0}-\left[\boldsymbol{K}\right]\left\{\boldsymbol{D}\right\}_{0}-\left[\boldsymbol{C}\right]\left\{\dot{\boldsymbol{D}}\right\}_{0}\right) \tag{31}$$

With Eqs (30a)-(30c) and (31), we can obtain $\left\{\boldsymbol{D}\right\}_{1}$, $\left\{\boldsymbol{D}\right\}_{2}$, $\left\{\boldsymbol{D}\right\}_{3}$, and so forth. From the above-mentioned details, it is obvious that the numerical calculation of TRA is more complicated than that of HRA and therefore requires more computation resources when the model being larger.

In TRA or HRA, we need to suppress reflections from the hard boundary to get rid of the unwanted resonance peaks. Based on the wave equation in spherical coordinate, artificial boundary can be equivalent to many continuous distribution parallel viscous-spring systems. The coefficients of stiffness and damping are given as follows:

$$K_{T}=\frac{\alpha_{T}G}{LN}\ ;\ K_{N}=\frac{\alpha_{N}G}{LN} \tag{32a}$$

$$C_{T}=\frac{\sqrt{G\rho}}{N}\ ;\ C_{N}=\frac{\sqrt{E\rho}}{N} \tag{32b}$$

where K_T and K_N are tangential and normal stiffness coefficients of springs, respectively; ρ is the material density of matrix silicon; C_T and C_N are tangential and normal damping coefficients, respectively; G and E are shear modulus and Young's modulus of matrix silicon, respectively; L and N are the distance from exciting source to artificial boundary and number of viscous-spring systems attached to the boundary, respectively; α_T and α_N are the tangential and normal modified coefficients for artificial boundary, respectively. α_T and α_N are assigned with 0.67 and 1.33, respectively [20].

2.4 Periodic structure without/with Substrate by SC-PWE method

The super-cell plane wave expansion (SC-PWE) method is another efficient way to calculate the plate-mode waves of the phononic crystal plates. As shown in Fig. 4, we establish a 3D

model in Cartesian coordination to calculate the elastic band structures of 1D phononic crystal plates, where the periodic composite plate consists of alternate *A* and *B* strips, *C* is the LIM layer, and *D* is the substrate, respectively [21].

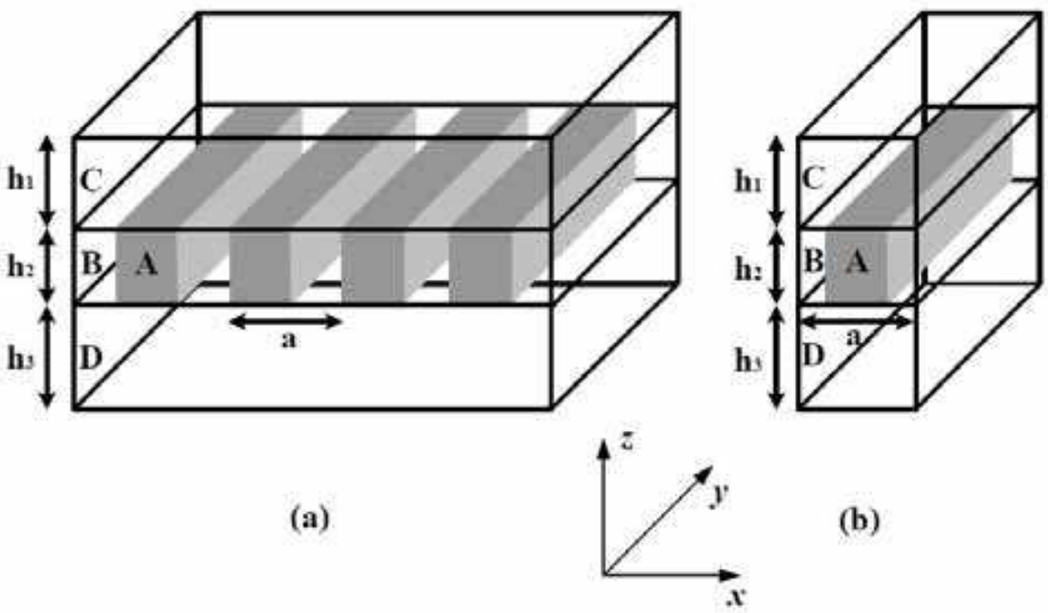

Fig. 4. (a) 1D Lamb wave phononic crystal plate sandwiched between two layers of homogeneous materials, and (b) 3D super-cell used in the computation.

The LIM is an imaginary material with relatively low elastic moduli for approximately meeting the requirement of free boundary condition and an extremely low mass density, which leads the sound speed in the LIM to be much larger than that in usual solid material. In this chapter, the LIM is assumed as an isotropic material with $C_{11} = 2 \times 10^6$ N/m², $C_{44} = 1 \times 10^6$ N/m², $C_{12} = 0$ N/m² and $\rho = 1 \times 10^{-4}$ kg/m³. The choice of such unphysical high sound speeds for the LIM is in good agreement with the numerical condition derived by Tanaka et al [22]. With these values, both good numerical convergence and computing accuracy can be achieved. The thickness of plate h is assumed to be 2 mm and $h = h_2 + h_3$ where $h_3 = 0$ mm for the case without substrate. The thickness of the LIM layer h_1 is defined to be $5h_2$ to reduce unexpected wave coupling between two nearest phononic layers in z direction [23]. In the absence of body force and strain in y direction, the SH mode wave in 1D plate can be decoupled. Regardless of the wave propagating in y direction, the elastic wave equations of phononic crystal are given by:

$$\rho(\boldsymbol{r})\ddot{u}_p = \partial_q[C_{pqmn}(\boldsymbol{r})\partial_n u_m] \quad (p = 1,2,3) \tag{33}$$

where $\boldsymbol{r} = (x,z)$. This equation can be solved by a standard Fourier expansion to $\rho(\boldsymbol{r})$, $C_{pqmn}(\boldsymbol{r})$ and $u(\boldsymbol{r},t)$, which are all position-dependent values. For convenience, we put $\alpha = (\rho, C_{pqmn})$ and then we can obtain the following equations:

$$\alpha(\boldsymbol{r}) = \sum_{\mathbf{G}_x} \sum_{G_z} \alpha_{\mathbf{G}} \exp[i(G_x x + G_z z)] \tag{34}$$

$$u(\boldsymbol{r},t)=\sum_{\boldsymbol{G}_x}\sum_{G_z}u_{\boldsymbol{G}}\exp[i(G_x x+G_z z)]e^{i(\boldsymbol{k}\cdot\boldsymbol{r}-\omega t)} \tag{35}$$

where $\boldsymbol{k}=(k_x,k_z)$ is the Bloch wave vector and the 2D reciprocal-lattice vector $\boldsymbol{G}=(G_x,G_z)$, respectively. Substituting equations (34) and (35) into wave equation (33), we can obtain:

$$\omega^2\begin{pmatrix}\rho_{\boldsymbol{G}-\boldsymbol{G}'} & & \\ & \rho_{\boldsymbol{G}-\boldsymbol{G}'} & \\ & & \rho_{\boldsymbol{G}-\boldsymbol{G}'}\end{pmatrix}u_{\boldsymbol{G}'}=\begin{pmatrix}M^{11}_{\boldsymbol{G},\boldsymbol{G}'} & M^{12}_{\boldsymbol{G},\boldsymbol{G}'} & M^{13}_{\boldsymbol{G},\boldsymbol{G}'}\\ M^{21}_{\boldsymbol{G},\boldsymbol{G}'} & M^{22}_{\boldsymbol{G},\boldsymbol{G}'} & M^{23}_{\boldsymbol{G},\boldsymbol{G}'}\\ M^{31}_{\boldsymbol{G},\boldsymbol{G}'} & M^{32}_{\boldsymbol{G},\boldsymbol{G}'} & M^{33}_{\boldsymbol{G},\boldsymbol{G}'}\end{pmatrix}u_{\boldsymbol{G}'} \tag{36a}$$

The explicit expressions of the matrix elements $M^{lm}_{\boldsymbol{G},\boldsymbol{G}'}$, ($l=m=1-3$) are:

$$\begin{aligned}
&M^{11}_{\mathbf{G},\mathbf{G}'}=C^{11}_{\mathbf{G}-\mathbf{G}'}(k_x+G'_x)(k_x+G_x)+C^{44}_{\mathbf{G}-\mathbf{G}}G'_zG_z && M^{12}_{\boldsymbol{G},\boldsymbol{G}'}=0\\
&M^{13}_{\boldsymbol{G},\boldsymbol{G}'}=C^{12}_{\boldsymbol{G}-\boldsymbol{G}}G'_z(k_x+G_x)+C^{44}_{\boldsymbol{G}-\boldsymbol{G}'}(k_x+G'_x)G_z && M^{21}_{\boldsymbol{G},\boldsymbol{G}'}=0\\
&M^{22}_{\boldsymbol{G},\boldsymbol{G}'}=C^{44}_{\boldsymbol{G}-\boldsymbol{G}'}(k_x+G'_x)(k_x+G_x)+C^{44}_{\boldsymbol{G}-\boldsymbol{G}}G'_zG_z && M^{23}_{\boldsymbol{G},\boldsymbol{G}'}=0\\
&M^{31}_{\boldsymbol{G},\boldsymbol{G}'}=C^{44}_{\boldsymbol{G}-\boldsymbol{G}}G'_z(k_x+G_x)+C^{12}_{\boldsymbol{G}-\boldsymbol{G}'}(k_x+G'_x)G_z && M^{32}_{\boldsymbol{G},\boldsymbol{G}'}=0\\
&M^{33}_{\boldsymbol{G},\boldsymbol{G}'}=C^{44}_{\boldsymbol{G}-\boldsymbol{G}'}(k_x+G'_x)(k_x+G_x)+C^{11}_{\boldsymbol{G}-\boldsymbol{G}}G'_zG_z &&
\end{aligned} \tag{36b}$$

where the Fourier coefficients $C^{pq}_{\boldsymbol{G}-\boldsymbol{G}'}$ are related to $C_{pqmn}(\boldsymbol{r})$ in a conventional manner. As shown in equation (36a), characteristic frequency ω is exactly the squared generalized eigenvalue of density matrix and elastic constant matrix. The coefficients $C^{pq}_{\boldsymbol{G}-\boldsymbol{G}'}$ and $\rho_{\boldsymbol{G}-\boldsymbol{G}'}$ takes the form:

$$\alpha_{\boldsymbol{G}-\boldsymbol{G}'}=\frac{1}{V_c}\iiint_{(Supercell)}\alpha(\boldsymbol{r})\exp[-i(\boldsymbol{G}-\boldsymbol{G}')\cdot\boldsymbol{r}]d^3\boldsymbol{r} \tag{37}$$

where V_c is the volume of super-cell. With the above-mentioned equations, we can easily obtain the band structure of 1D phononic crystal plate.

2.5 Quasiperiodic structure by FE method

As shown in Fig.5, the quasiperiodic composite plate consists of material A of width d_A and material B of width d_B. The lattice spacing is $D=d_A+d_B$. When the distribution of materials A and B is arranged according to the Fibonacci sequence, one obtains a quasiperiodic system [24]. We create the Fibonacci sequence *B*, *BA*, *BAB*, *BABBA*, *BABBABAB*, *BABBABABBABBA*, … according to the production rule $S_j=S_{j-1}\,|\,S_{j-2}$ for $j\geq 3$ with $S_1=B$ and $S_2=BA$. When A and B are put along the chain alternately, a periodic model is obtained. We introduce parameter $\Phi=d_A/d_B$ to describe the ratio of the two components. Φ is fixed at 1.0 and the number of layers N is 13 throughout the section unless otherwise stated. The wave propagates along the x direction of the plate bounded by planes $z=0$ and $z=L$. We consider a 2D problem, in which all field components are assumed to be y independent.

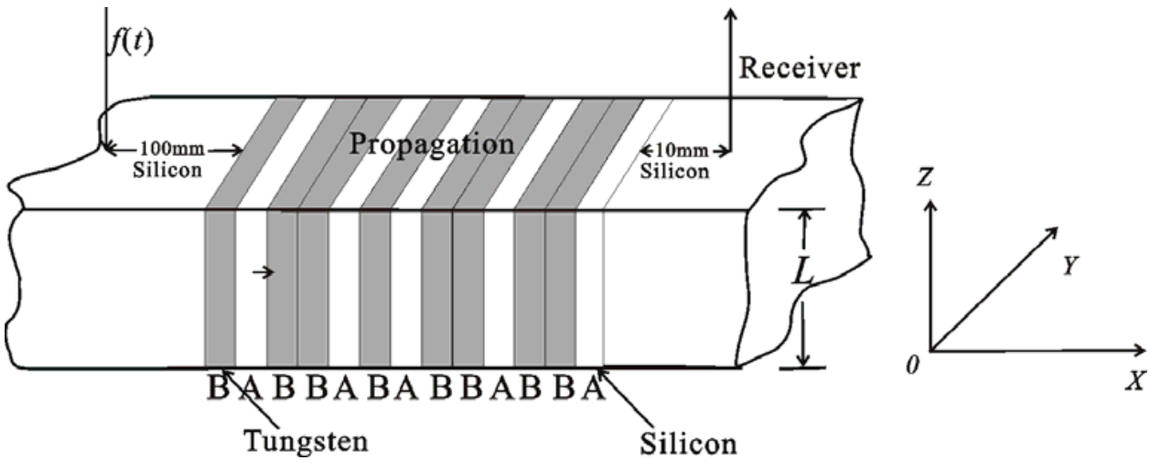

Fig. 5. The configuration of 1D quasiperiodic composite plate consisting of Tungsten and Silicon strips arranged following the Fibonacci sequence.

To demonstrate the structures of the band gaps for Lamb waves in the 1D quasiperiodic systems and the difference from that of periodic systems, we calculate TPS of the transient Lamb waves by using the TRA. We suppose that a Lamb wave is excited by a line laser pulse with a spatial Gaussian distribution (Gaussian radius = 0.2 mm). The laser pulse, which is normally incident to the surface of the studied plates, generates the Lamb wave propagating along the x direction. The laser-generated force source $f(t)$ is simulated as a delta function, which is perpendicular to the surface of the plate [25].

The elastic properties of the materials in the numerical calculations are the same as mentioned in above sections; and the thickness of the plates (L) of 1.0 mm. The step sizes of temporal and spatial discretization in the FE calculations are fine enough for the convergence of the numerical results. Lamb waves are excited by the force function $f(t)$ at x=0, and are received at the point 10 mm away from the superlattices array. The generation source is far from the Fibonacci superlattices in order to obtain approximately plane waves when the wave fronts reach the plate. The received vertical displacement in time domain is Fourier-transformed into the frequency domain to yield the TPS.

We also adopt the HRA to study three quasiperiodic systems. Two Generalized Fibonacci Systems (Type A and Type B) [26] are obtained inductively through the following transformations:

$$A \to AAB,\ B \to A \quad \text{for Type A Fibonacci System} \tag{38a}$$

$$A \to ABB,\ B \to A \quad \text{for Type B Fibonacci System} \tag{38b}$$

We can generate the two quasiperiodic systems, as shown as follows:

$$AABAABAAABAABAAABAAB\ldots \text{ for Type A Fibonacci System} \tag{39a}$$

$$ABBAAABBABBABBAAABBA\ldots \text{ for Type B Fibonacci System} \tag{39b}$$

It is interesting to find out that Generalized Fibonacci Systems are very flexible in forms and by changing the transformations ($A \to ABA$, $B \to A$ …) we can obtain many other quasiperiodic systems.

Then, we can introduce the third quasiperiodic system (Double-period System) into this model. The recursion relation for Double-period System is $A \to AB$, $B \to AA$ [27]. With the recursion relation, we can obtain the sequence of the Double-period System:

ABAAABABABAAABAAABAA…for Double-period System (40)

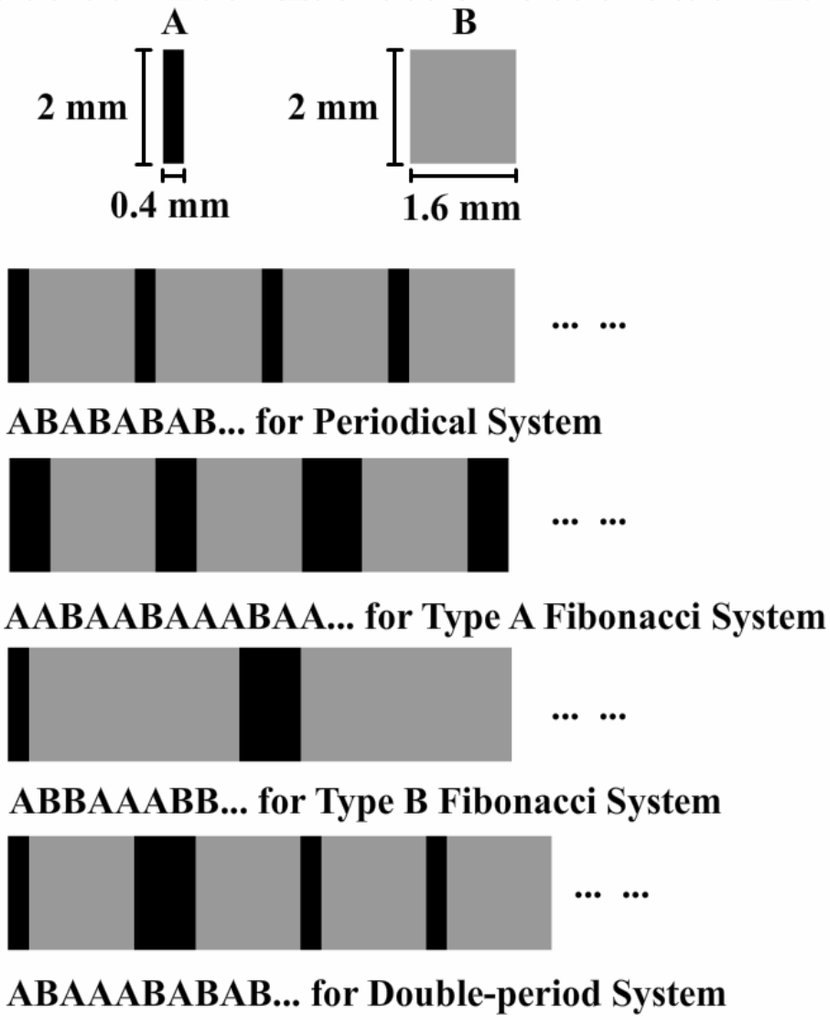

Fig. 6. The schematic diagram of the four systems: Periodic System, Type A Fibonacci System, Type B Fibonacci System and Double-period System, respectively.

Fig. 6 shows the scheme of the four different systems, namely, Periodic System, Type A Fibonacci System, Type B Fibonacci System and Double-period System, respectively. In numerical simulations, the homogeneous media A and B are gold and silicon, with the thicknesses of media A and B are 2 mm, and the widths of media A and B are 0.4 and 1.6 mm, respectively.

3. Lower-order lamb waves in 1D composite thin plates without/with substrate

In order to demonstrate the existence of band gaps for low-order Lamb wave modes in the 1D periodic structure as shown in Fig.1, we have calculated the dispersion curves for a cubic medium (silicon) of a 1 mm thick plate by considering only the fundamental term in the Fourier and Floquet series [16], as shown in Fig. 7(a). Fig. 7(b) displays the dispersion

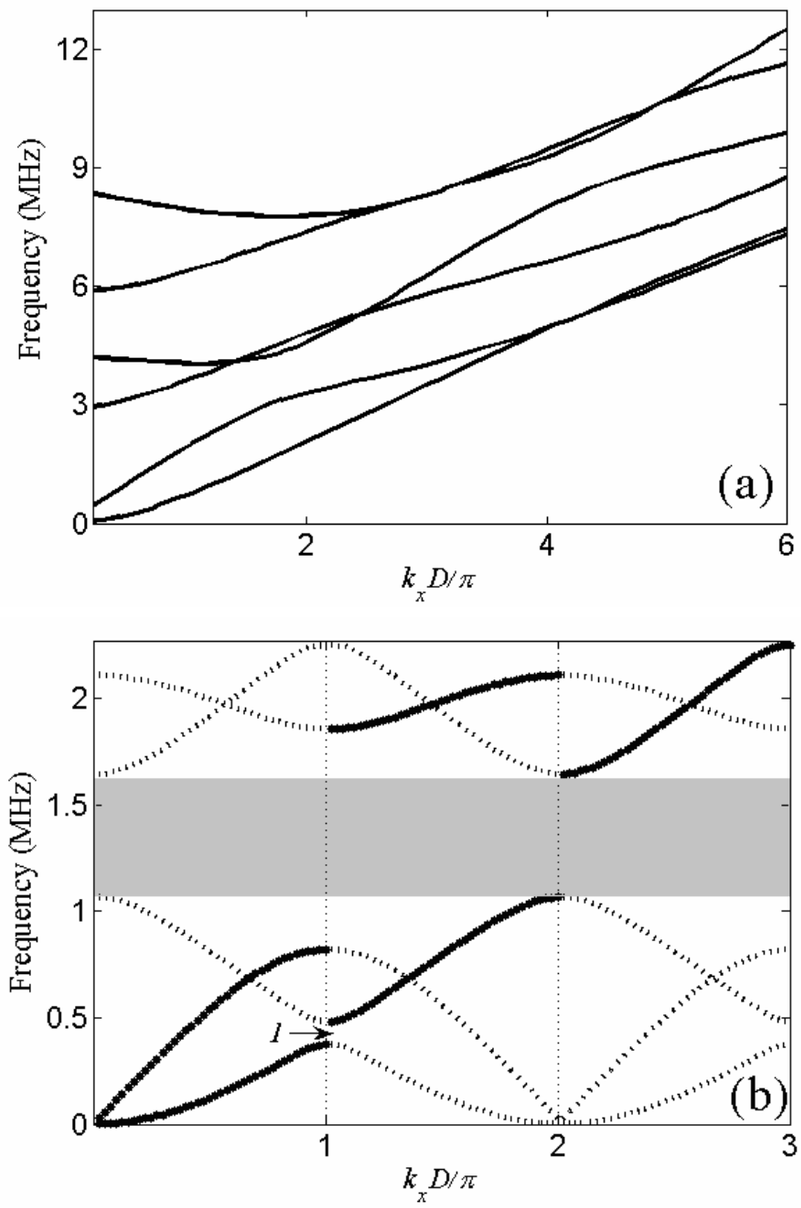

Fig. 7. Schematic representation of the Lamb wave dispersion curve for (a) a homogeneous Si plate with $L = 1.0$ mm (b) composite thin plate (W / Si) with $f = 0.5$, $L = 1.0$ mm, and $D = 2.0$ mm.

curves of four lower-order modes along the boundary of the mini-Brillouin zone with filling ratio $f = 0.5$, $L = 1.0$ mm, and $D = 2.0$ mm. One can obviously observe the modifications produced by resonant reflections in the strip lattice. The dashed vertical line identifies the frequency zone where all the Lamb wave modes are resonantly reflected by the periodic lattice of strips. The proposed approach allows one to identify that the forward propagating Lamb wave modes are not coupled with the backward propagating modes.

By comparing Fig. 7(a) with Fig. 7(b), one can easily find that there exists a band gap from 1065 to 1642 kHz for the lower-order Lamb wave modes propagating in the 1D periodic structure. The gap width ($\Delta\Omega$) is 577 kHz and the corresponding gap/midgap ratio ($\Delta\Omega / \Omega_m$, Ω_m is the midgap frequency) is approximately 0.426. In order to analyze the influence of the ratio L/D for the band gap width, we also calculate the dispersion curves of the lower-order modes with $f = 0.5$, $L = 2.0$ mm, and $D = 2.0$ mm, as shown in Fig. 8. It is apparent that there are two band gaps (from 806 to 1167 kHz and from 1438 to 1863 kHz, respectively) for the ratio $L/D = 1$. The gap widths are 361 and 425 kHz, and the corresponding gap/midgap ratios are about 0.366 and 0.255, respectively.

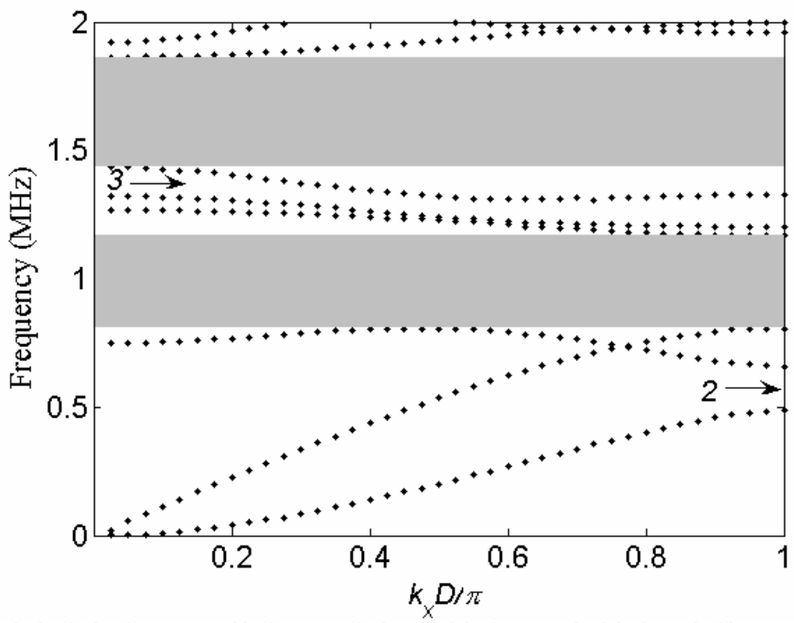

Fig. 8. Dispersion curves of Lamb wave modes for 1D finite thickness composite plate with filling ratio $f = 0.5$, $L = 2.0$ mm, and $D = 2.0$ mm.

Basically, there are three parameters that influence the formation of band gaps, i.e., L/D, f, and the contrast between the physical parameters of the constituents. It is rather intuitive that L/D is very crucial for the formation of a band gap. If it is either too small or too large, there should be no band gaps for lower-order modes. Fig. 9 depicts the gap width of the lowest band gap as a function of L/D with $f = 0.5$ and $D = 2$ mm for tungsten/silicon supperlattices. It is noteworthy to point out that the lowest band gap opens up over a domain of the ratio of L/D defined by $0.15 \le L/D \le 1.64$. The maximum value of gap width appears at $L/D \approx 0.53$ for the lowest band gap and reaches 610 kHz as shown in Fig. 9.

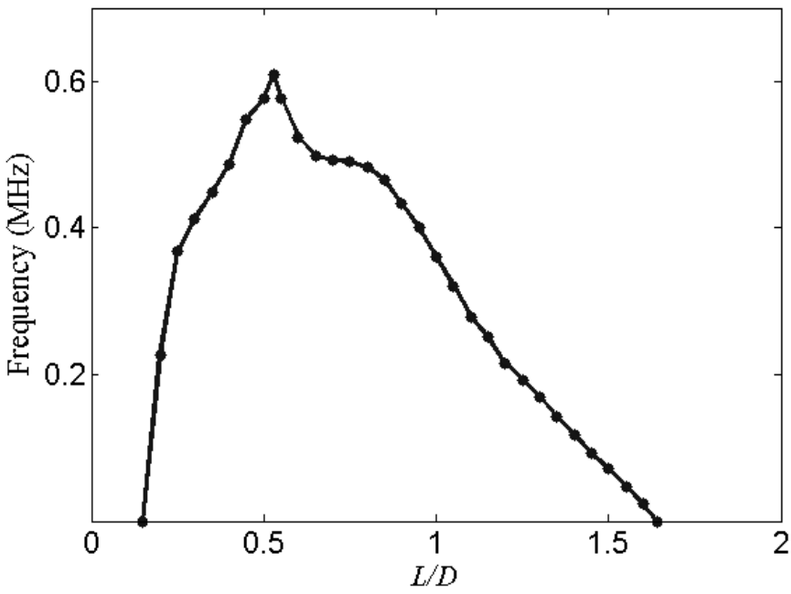

Fig. 9. The width of the lowest band gap at the filling fraction f = 0.5 versus the value of L/D.

It is noted that the value of the normalized gap width of the lowest band gap in the systems increases progressively with the increase of the value of the ratio of L/D until a critical value and then decreases. In fact, a plate can support a number of Lamb wave modes depending on the value of the ratio L/λ, where λ is the acoustic wavelength. When the periodicity of these Lamb waves matches the lattice spacing, stop bands appear in the Lamb wave dispersion curves [28]. There is a high interaction when the wavelength of Lamb wave is close the lattice constant, which induces mode conversion and reflections. When the wavelength of Lamb wave is different from the periodicity of the lattice constant, the interaction is weak. On the another hand, the midgap frequency of forbidden gap is inversely proportional to the lattice constant D [29], therefore, the value of the ratio of L/D is important for the width of the band gap for the Lamb waves in the periodic composite systems.

In order to demonstrate further the existence of the band gaps for the lower-order modes in the 1D periodic structure, the finite element method (FEM) is employed to calculate the transmitted power spectra (TPS) for the finite periodic structure as shown in Fig.3.

Fig. 10 shows the TPS for the 1D composite structure plate with $f = 0.5$, $L = 1.0$ mm, and $D = 2.0$ mm. There is a broad region from 1060 to 1630 kHz that is less than –30dB. The result shows good agreement with that by PWE method. The TPS is also depicted in Fig. 10 from a pure Tungsten plate with the same dimensions, and no sharp attenuation in any frequency domain is observed.

For the second sample, f, D, and the configuration are the same with the first one, and only the thickness of the plate is different (L=2 mm). Fig. 11 depicts the TPS for 1D plate with periodic structure and without periodic structure. The frequency range of the gaps of Lamb waves by PWE is almost the same with those of large attenuation in the calculated TPS .The first gap extends from the frequency of 804 up to 1176 kHz and the second from 1436 to 1869 kHz, which are less than –45dB.

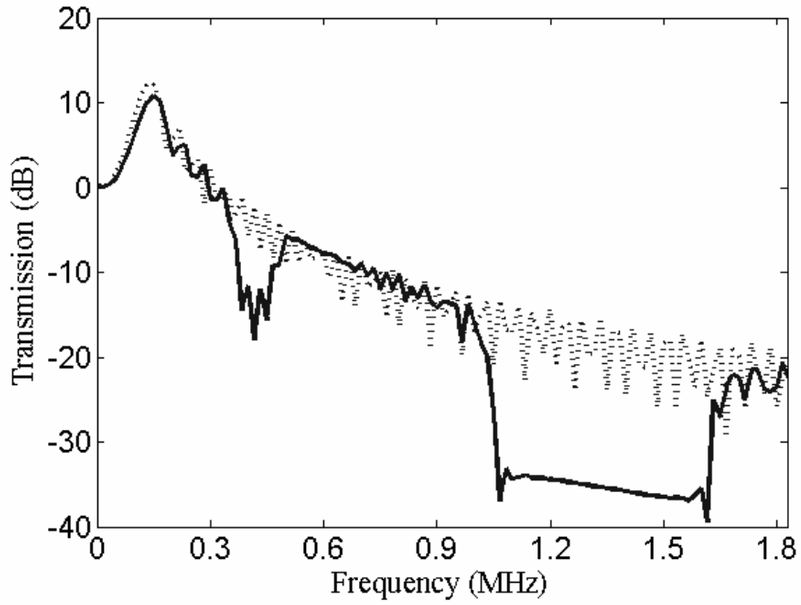

Fig. 10. The TPS computed by the FE method with $f = 0.5$, $L = 1.0$ mm, and $D = 2.0$ mm through the composite pate (solid line) and a pure Tungsten plate (dashed line).

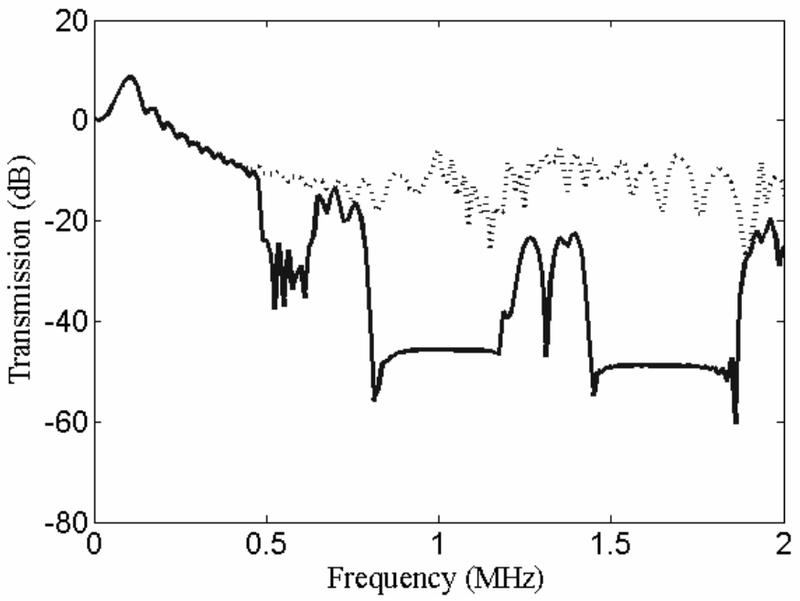

Fig. 11. The TPS computed by the FE method with $f = 0.5$, $L = 2.0$ mm, and $D = 2.0$ mm: through the composite plate (solid line) and through a pure Tungsten plate (dashed line).

It is interesting to notice that there are some slight dips centered at about 0.4MHz in Fig. 6, or 0.5MHz and 1.3MHz in Fig. 11. These dips attribute to the band gaps of antisymmetric modes, but not absolute band gap of both symmetric and antisymmetric modes, which can be observed in Figs. 7(b) and 8, indicated by the arrows 1, 2 and 3. On the other hand, the

lower frequency components of the modes is mainly excited for the thin plate [30], so that the TPS energy displays a monotonic decrease as the frequency increases as shown in Fig. 10. When the plate is thicker, the higher frequency components increase, which makes the attenuation of the TPS energy less, as shown in Fig. 11.

Since various modified photonic crystal structures, such as regular arrangements of individual metal nanoparticles on dielectric substrate, have been the subject of extensive research in recent years, it is meaningful to study the elastic modes in the system with PC layer coated on uniform substrate [31]. In fact, from the application point of view, when the thickness of the periodic thin plate is of the order of magnitude of several hundred micrometers, one needs to use substrate to support such a plate. Therefore, the effect of the substrate is important and cannot be neglected.

We study the influence of substrate on the band structure of the Lamb wave in PC layer by FEM. We also employ V-PWE to calculate the dispersion curves of Lamb wave. As we shall demonstrate that the locations and widths of band gaps on the dispersion curves from the V-PWE method are in good agreement with the results from the TPS by FEM.

In order to demonstrate the influences of different substrates on band gaps in the PC layer with substrate, we study three types substrate: hard material (Tungsten), soft material (Rubber) and medium hardness material (Silicon). The corresponding TPS (in green, blue, and red, respectively) are shown in Fig. 12 (a-b) for different h_2. For comparison, we also show the case without substrate (black).

It can be easily seen that there exist two band gaps for the Lamb modes propagating in the 1D periodic model. The first gap extends from the frequency of 820 kHz up to 1160 kHz and the second one from 3050 kHz to 3360 kHz, which is less than –38 dB, as shown in Fig. 12 (black line).

Comparing the TPS of the 1D PC layer without substrate (black line) with that of coated Tungsten substrate (green line) [Fig. 12(a)], we can see that the width of the first band gap decreases to some slight dips centered at about 1.0MHz (green line). The second band gap has a little decay in frequency domain (from 2850 to 3250 kHz). This demonstrates that the influence of hard substrate on band gaps is strong even when the substrate is very thin. The band gaps disappear rapidly when the substrate becomes thicker as shown in Fig. 12(b). It is because when the substrate becomes thicker, more energy will go via the substrate instead of via the PC, so that the interference from different periodic layers becomes less important.

The TPS for the 1D PC layer coated on Rubber substrate with different thickness h_2 are also shown in Fig. 12(a-b) (blue line). It is seen that there is no obvious change in the band gaps when the substrate is thin, especially, for the first band gap at low frequency region. However, as the thickness of substrate increases, interesting things happen, as shown in Fig. 12(b) (h_2=0.5mm). The band gap in the PC layer coated on Rubber substrate does not disappear but becomes smoother in the band gaps domain. Three band gaps appear, namely, from 750 kHz up to 1200 kHz, from 1720 kHz up to 1950 kHz and from 2920 kHz up to 3640 kHz, respectively. Compared with the band gap of the PC plate without substrate, we can see a broad band appears in the range of 1720 kHz and 1950 kHz. From Fig. 12(b), it is clearly seen that more band gaps appear, such as some band gaps in low frequency domain, which is opposite to the hard substrate. The appearance of more bands is due to the more interference from the boundary as Rubber is softer than Tungsten and Silicon, therefore there is more reflection at the interface between the PC and the substrate.

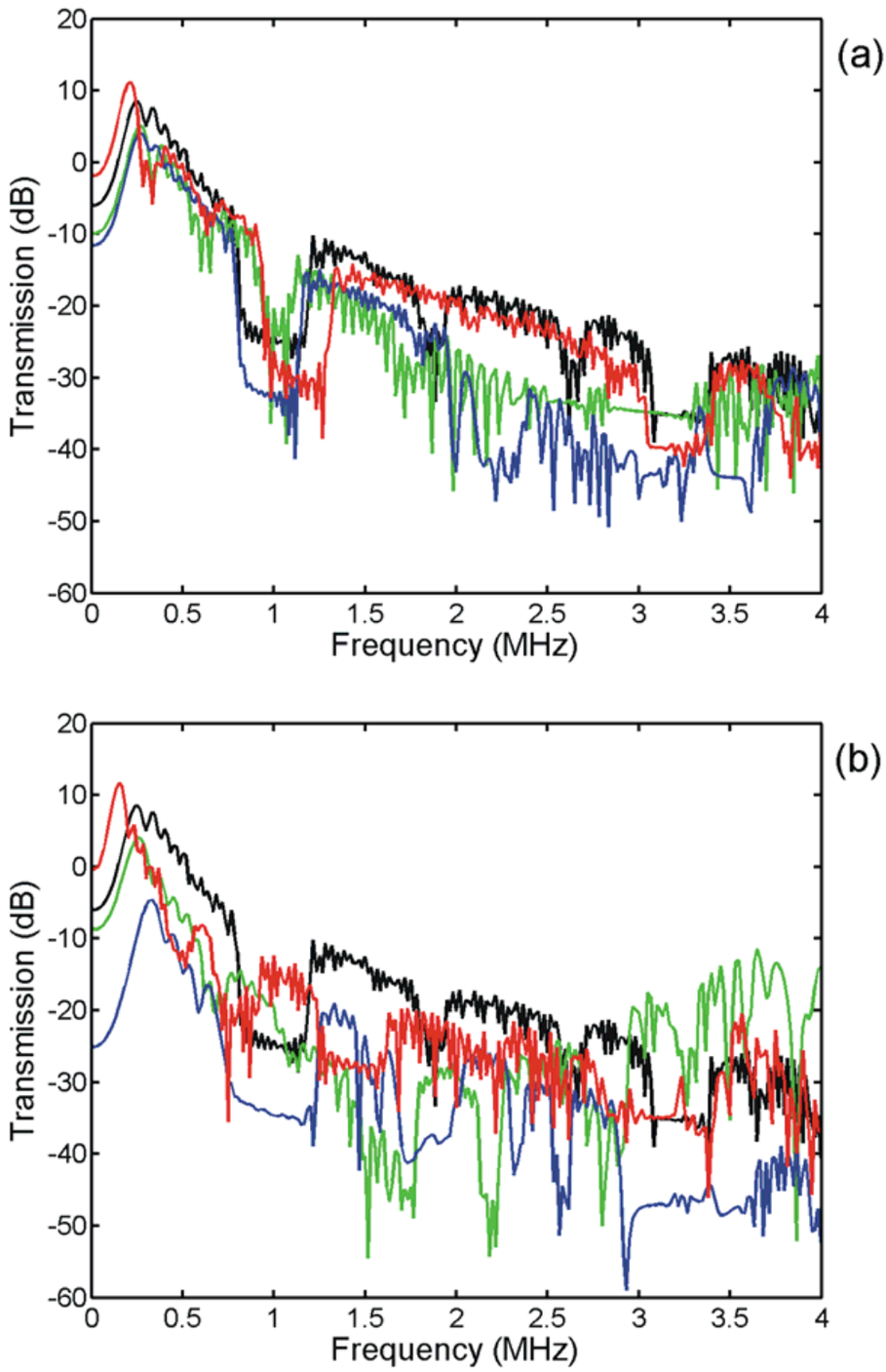

Fig. 12. (color online) The TPS for the 1D PC layer without substrate (black line), and for the 1D PC layer coated on Tungsten substrate (green line), Rubber substrate (blue line), Silicon substrate (red line), respectively, with different h_2 : (a) $h_2 = 0.125$ mm; (b) h_2=0. 50 mm

We also show the TPS for the 1D PC layer coated on Silicon substrate with different substrate thickness h_2. From Fig. 12(a) (red line), it can be easily found that there exist two band gaps for the Lamb modes propagating in the 1D PC layer coated on Silicon substrate. The first gap extends from 920 kHz up to 1280 kHz and the second from 3050 kHz to 3400 kHz, which are less than –40dB. Compared with Fig. 12(a) (black line and red line), we can see there is no obvious change between the band gaps when the substrate is thin. Although there are some band gaps appearing like some band gaps in low frequency domain when the thickness of substrate increases, the depth of band gap decreases. For example, one can see that although there is a band gap at about 1.5 MHz, the depth of band gaps for the model of Silicon substrate becomes very small as the thickness of substrate increases. Therefore, the influence of the Silicon substrate is between those of the hard substrate and the soft substrate.

To verify our numerical results, we calculate the dispersion curves of Lamb wave modes propagating along the x direction in the presence of the uniform substrate by V-PWE method.

Fig. 13 displays the dispersion curves of the lower-order modes of the 1D PC layer coated on Silicon substrate with different substrate thickness h_2. It is apparent that there are two band gaps (from 980 to 1285 kHz and from 3020 to 3380 kHz, respectively) for the h_2=0.125mm, as shown in Fig. 13(a). The gap widths are 305 kHz and 360 kHz, respectively, and the corresponding gap/mid-gap ratios are about 0.269 and 0.112, respectively. The results calculated by the V-PWE method show that the locations and widths of band gaps on the dispersion curves are in good agreement with the results on the transmitted power spectra by FEM, as shown in Fig. 12(a) (red line).

Some band gaps appear in low frequency domain with the increase in the thickness of substrate, which is also found by V-PWE method. For example, we can see that there are three band gaps (from 685 to 820 kHz, from 1320 to 1590 kHz and from 3120 to 3250 kHz) for the model of Silicon substrate with the thickness of 0.5mm as shown in Fig. 13(b), which is in good agreement with the results by FEM as shown in Fig. 12(b) (red line).

Here, we give a qualitative physical explanation of above results. When the substrate is Tungsten material, because the ratio of acoustic impedances of Tungsten and Silicon $\rho_S C_S / \rho_T C_T \approx 0.2$ (where ρ_S (C_S) and ρ_T (C_T) are the mass densities (the acoustic velocities of longitudinal wave) of Silicon and Tungsten, respectively), the interface between the PC layer and the substrate is equivalent to a hard boundary condition, at which the phase change of the reflected wave pressure is less than 90°. The superposition of the reflective wave will destroy the formation condition of band gap, as the formation of band gap is due to the destructive interference of the reflective waves. Therefore, the influences on band gaps are significant even when the substrate is very thin. On the other hand, due to the interface is not strictly strong, the Lamb wave can transmit partially to the uniform substrate, and then the band gaps disappear rapidly when the substrate becomes thicker.

In contrast, when the substrate is Rubber material, because the acoustic impedances of Silicon is approximately seven times of that of Rubber, the interface between the PC layer and the substrate can be approximately considered a soft boundary, at which the phase change of the reflected wave is larger than 90°. The superposition of the reflective waves will lead to the band gap. As the substrate is very thin, the influences on band gaps are negligible. On the other hand, as the interface is not strictly a pressure-released boundary, the Lamb wave can transmit partially to the uniform substrate. Because the mass density

and the elastic constants of Silicon are much larger than that of Rubber, the acoustic wave will be localized in the soft Rubber material. Therefore, band gaps become deeper as the thickness of substrate increases. If the substrate is Silicon, which is the same as the matrix material, the acoustic wave does not reflect at $z = 0$, In this case, the influence of the substrate is between those of the hard substrate and the soft substrate.

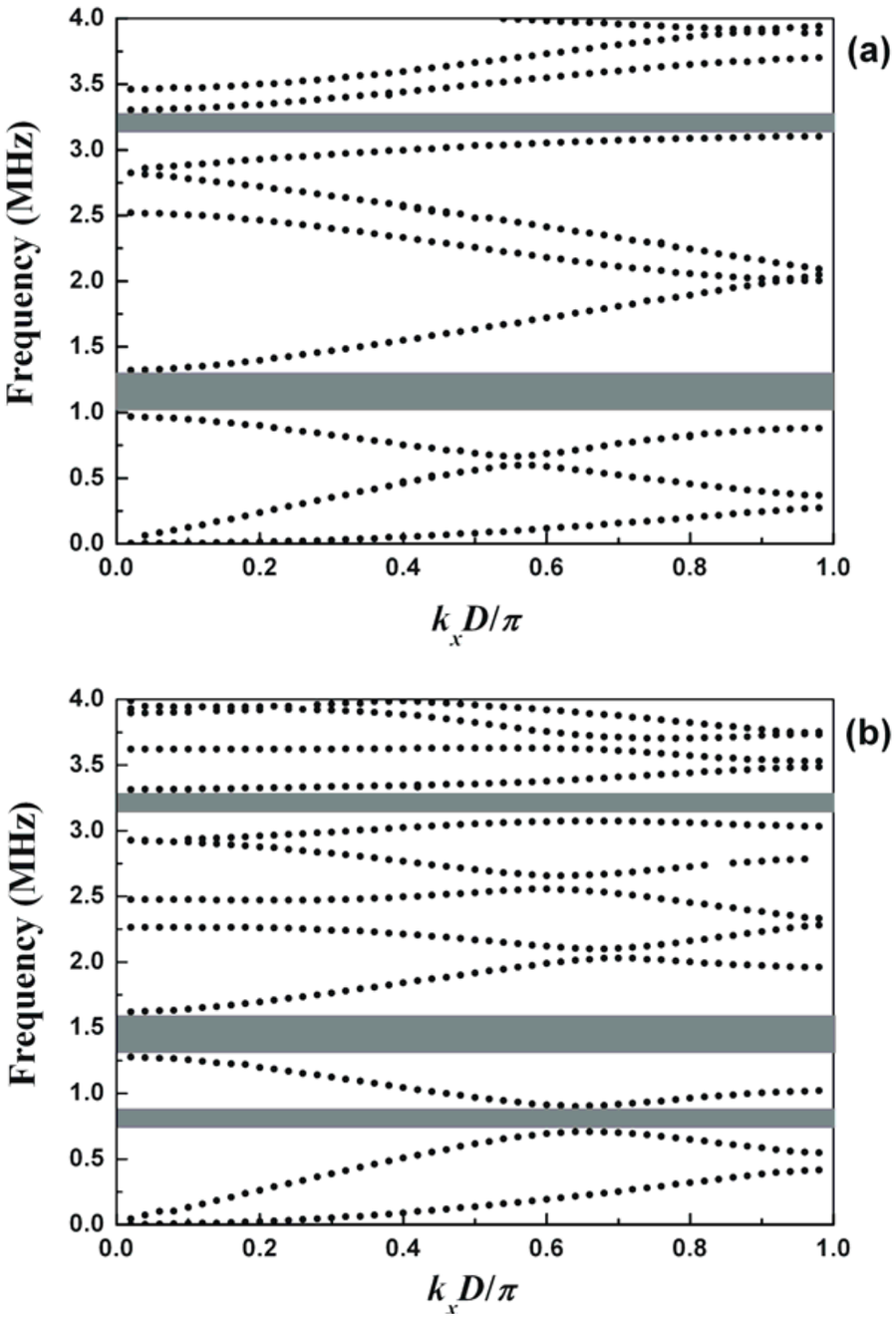

Fig. 13. The dispersion curves of Lamb modes of the 1D PC layer coated on Silicon substrate with different h_2 : (a) h_2=0.125 mm; (b) h_2=0.50 mm

4. Lamb waves in 1D quasiperiodic composite thin plates

In this section, we study numerically the band gaps of Lamb waves in 1D quasiperiodic thin plate. The motivation of the study lies in the factor that a lot of real-world materials are quasiperiodic [32-33]. In particular, since Merlin et al.[34] reported the realization of Fibonacci superlattices, a lot of interesting physical phenomena have been observed in x-ray scattering spectra, Raman scattering spectra, and propagating modes of acoustic waves on corrugated surfaces [35-37].

First, we show the dependence of TPS on L/D. From Fig. 14(a-e), the TPS are shown for the periodic and quasiperiodic composite plates with L/D= 0.3, 0.5, 0.54, 0.6, and 0.68, respectively. For comparison, the TPS for a pure Silicon plate of 1 mm thickness is also shown in order to demonstrate the band gaps. Fig. 14(a) shows that for such a pure silicon plate there is no band gap at all. However, two band gaps are clearly seen in the periodic system. The first band extends from frequency of 570 up to 760 kHz and the second one from the 1550 up to 1960 kHz. With the same parameters, the two bands are not so obvious in a quasiperiodic plate.

When L/D is increased to 0.5 [see Fig. 14(b)], interesting things happen. It is evident that for the periodic model there exists a band gap from 1050 up to 1615 kHz. However, for the quasiperiodic plate, a clear band split is seen from 1085 up to 1286 kHz and from 1460 up to 1710 kHz, and a new band appears in the range of 2010-2275 kHz.

As L/D is increased to 0.54 [Fig. 14(c)] and 0.6 [Fig. 14(d)], the only band gap in the periodic system does not change too much; it just shifts a little toward the high frequency. However, the situation changes in the quasiperiodic system. In the case of $L/D = 0.54$, the band gap is split into two subbands, namely, from 1210 up to 1380 kHz and from 1505 up to 1780 kHz. Two more new bands appear from 2050 up to 2420 kHz and from 2750 up to 2950 kHz. In the case of $L/D = 0.6$, only two bands appear, namely, from 1360 up to 1949 kHz and from 2205 up to 2685 kHz.

From the results shown in Figs. 14(a)-(d), we can say that the band structures of a quasiperiodic system depend strongly (or sensitively) on the parameter L/D, whereas that in a periodic system does not. A quasiperiodic system has more forbidden gaps than that a periodic system has. This can be explained from the following. The 1D Fibonacci sequence is the project of the 2D square periodic lattice; it implicitly includes the periodicity of a multidimensional space. In fact, a quasiperiodic structure may be considered as a system made up of many periodic structures [38].

Moreover, the change of the ratio L/D also leads to the changes of the number of splitting band gaps. Physically, as the ratio L/D changes to an appropriate value, due to reflections at the plate boundaries, the interaction between longitudinal and transversal strain components becomes strong. For the Lamb modes, the restriction of boundary conditions leads to intermode Bragg-like reflections in the quasiperiodic superlattices [39]. As a result, much more physical phenomena are present compared with the bulk wave propagation in the Fibonacci chains.

In general, there are three parameters that influence the formation of band gaps, namely, L/D, Φ, and λ (the acoustic wavelength). The number of Lamb wave modes in a plate depends on the value of L/λ. The midgap frequency of forbidden gap is inversely proportional to the lattice spacing D [29]. Therefore, it is rather intuitive that L/D is very crucial for the formation of band gaps for Lamb waves. In fact, it is also found that the difference between the forbidden gaps in quasiperiodic and periodic systems disappears

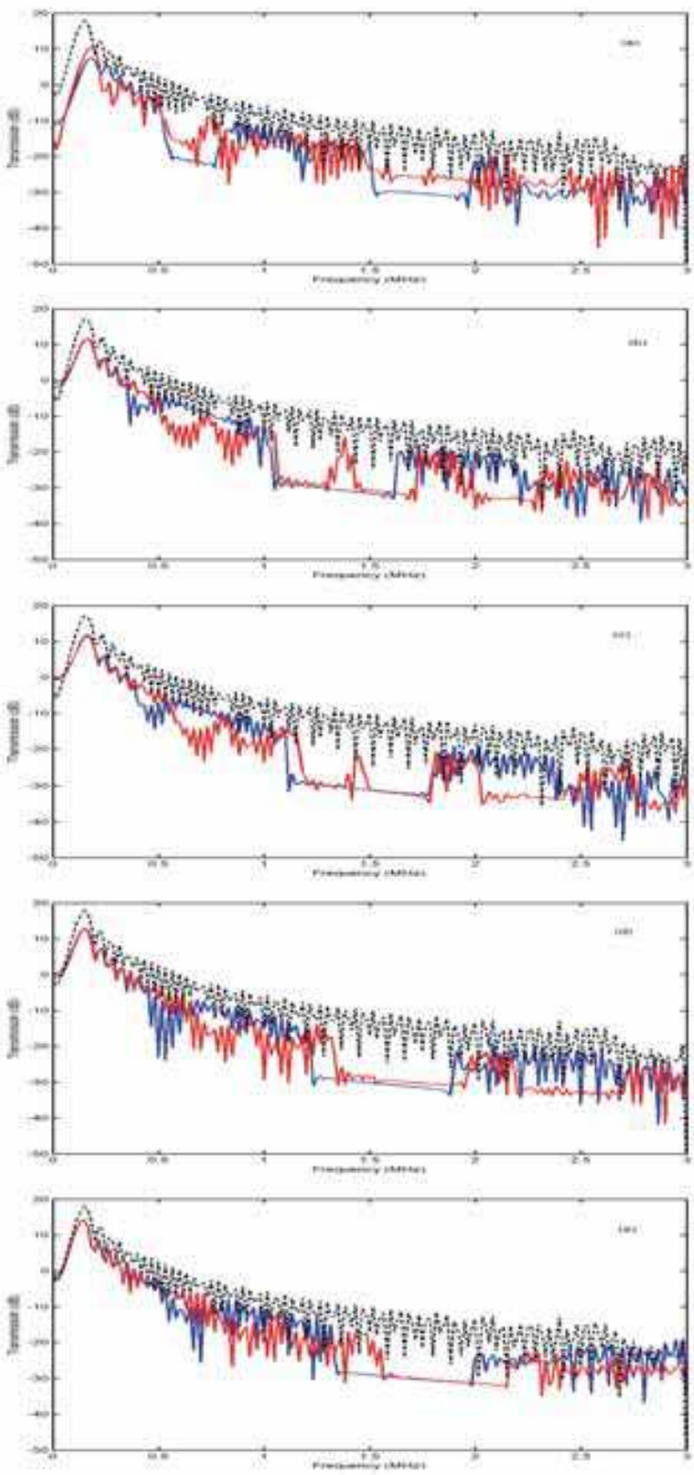

Fig. 14. (color online) The TPS for the periodic plate (blue), the quasiperiodic plate (red), and a pure Silicon plate (dashed black), respectively. (a) L/D=0.3, (b) L/D=0.5, (c) L/D=0.54, (d) L/D=0.6, (e) L/D=0.68.

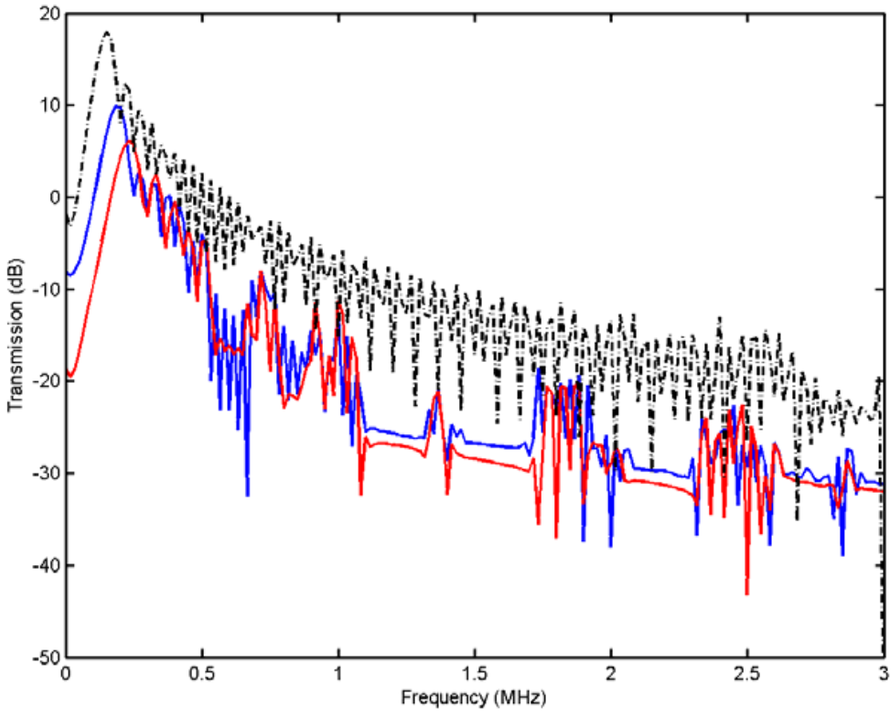

Fig. 15. (color online) The TPS of the quasiperiodic plate with N=21 (blue) and N=34 (red), and a pure Silicon plate (dashed black); L/D =0.5.

when the ratio L/D is larger than 0.68, as shown in Fig. 14(e). In this figure, one can see that there is only one forbidden gap in both the periodic and quasiperiodic systems. The gap extends from 1350 (1570) up to 1970 (2136) kHz for the periodic (quasiperiodic) system, respectively. It means that the difference of band gaps between quasiperiodic and periodic systems basically disappears as the lattice spacing decreases.

Furthermore, in order to investigate the finite size effect on band gaps, we calculate the TPS for $N = 21$ and 34 for $L/D = 0.5$. The results are shown in Fig. 15, which tells us that the number of splitting band gaps in quasiperiodic superlattices does not increase with the addition of the layer number of Fibonacci sequences. The result is quite different from those in the quasiperiodic photonic and phononic crystals of the bulk waves [40-41].

Lastly we study the influence of the thickness of sublattices on the band gap. We calculate the TPS for the cases of $d_A/D = 0.618$ and $d_B/D = 0.618$. The results are shown in Fig. 16. There is only one band gap in the structure of $d_A/D = 0.618$ ($d_B/D = 0.382$). The gap extends from the frequency of 1565 up to 1790 kHz. However, four band gaps are observed in the systems with $d_A/D = 0.382$ ($d_B/D = 0.618$). The four bands are from 950 up to 1130 kHz, from 1310 up to 1550 kHz, from 1780 up to 2030 kHz, and from 2250 up to 2530 kHz, respectively. One can easily find that the material (Tungsten) with larger values of the elastic constant and mass density influences the band gap more than the material (Silicon) with smaller values of the elastic constant and mass density.

In conclusion, we have examined the band gap structures of Lamb waves in the 1D quasiperiodic composite thin plates by calculating the TPS from the FEM. The band gap structures of the Lamb waves are quite different from those of bulk waves. Specifically, the

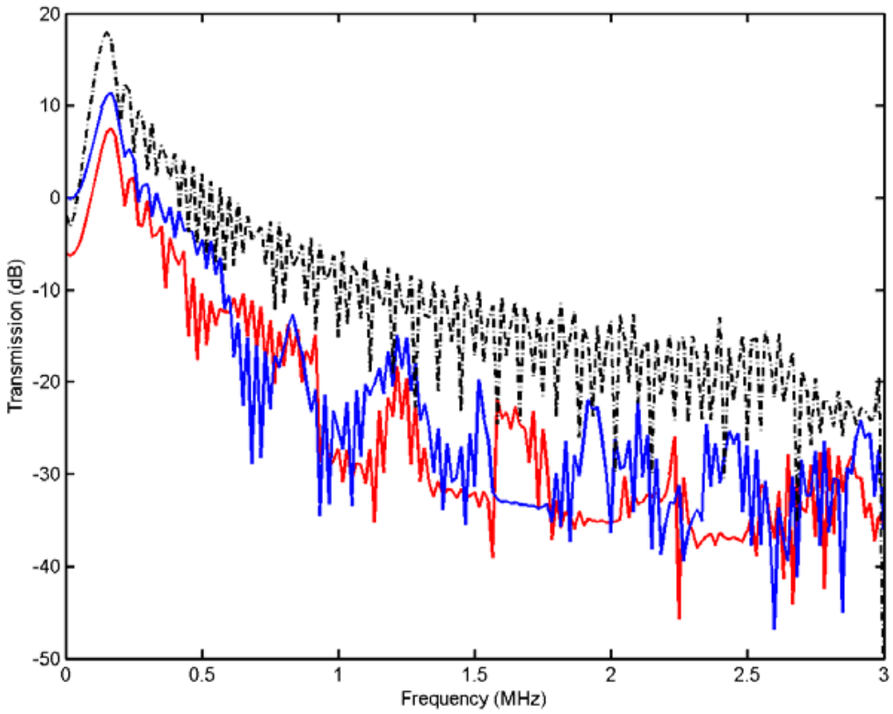

Fig. 16. (color online) The TPS of the quasiperiodic plate $d_A / D = 0.618$ (blue) and $d_B / D = 0.618$ (red), and a pure Silicon plate (dashed black); L/D =0.5.

number of splitting band gaps depends strongly on the values of L/D owing to resonance of the coupling of the longitudinal and transversal strain components at the plate boundaries. However, the split of band gaps is independent of the layer number of Fibonacci sequences. Moreover, we have found that the structure of the band gaps depends very sensitively on the thickness ratio of the sublattices A and B in the quasiperiodic structures which might find applications in nondestructive diagnosis.

5. Acoustic wave behavior in silicon-based 1D phononic crystal plates

In this section, we employ HRA to study the propagation and transmission of acoustic waves in silicon-based 1D phononic crystal plates without/with substrate. We also employ HRA to study quasiperiodic systems such as Generalized Fibonacci Systems and Double-period System, and the results show that some new phononic band gaps form in quasiperiodic systems, which hold the potential in the application of acoustic filters and couplers.

In Fig. 17, the parameters of finite element models for both TRA and HRA are set to be: the plate thickness $H = 2$ mm, the distance from exciting source to the left edge of plate (also the distance from the receiver to the right edge of plate) $L_1 = 15$ cm, the length of superlattice $S = 20$ cm, the number of finite elements per meter $N = 10000$ m^{-1}, the distance between exciting source and receiver $L_2 = 30$ cm, the width of the exciting source region (source function is Guassian function) $\delta = 4$ mm. In fact, the theoretical models for TRA and HRA are analogous to laser-generated Lamb wave system and piezoelectricity-generated Lamb wave system, respectively.

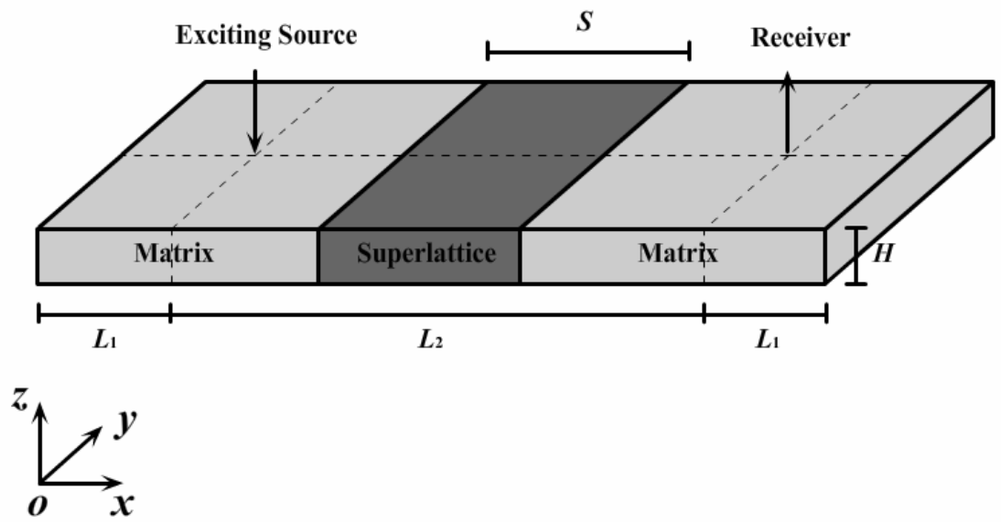

Fig. 17. The plate geometry in the finite element models for both TRA and HRA method; the upper surface is located at $z = H$.

We choose two cases (without/with substrate and different quasiperiodic systems) to investigate the acoustic wave behavior in phononic crystal plates.

For the plate without substrate, we set filling factor $f = 0.2$, lattice constant $a = 2$ mm, plate thickness $H = 2$ mm, without substrate. The number of inclusions is 100 and all the inclusions are embedded periodically in the middle of plate.

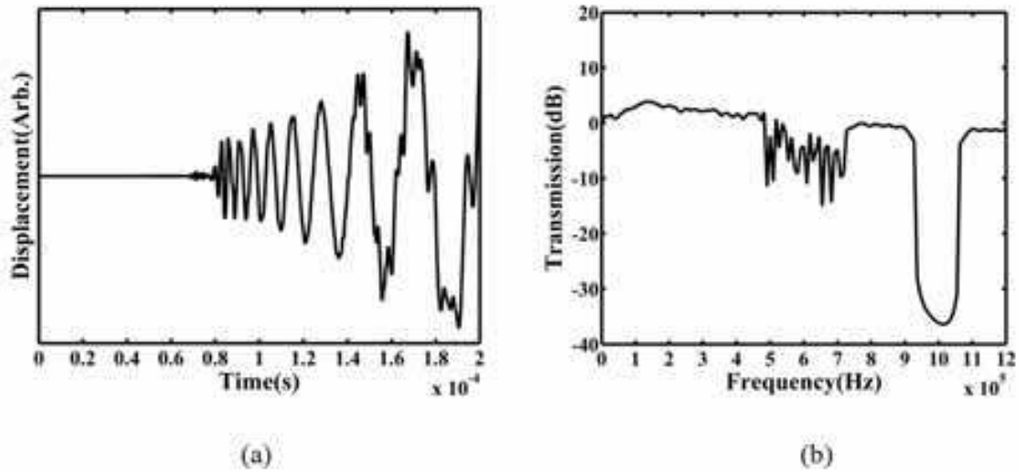

Fig. 18. (a) The transient vertical displacement at the upper surface of phononic crystal plate without substrate, calculated by TRA method; (b) Normalized transmitted power spectrum for phononic crystal plate without substrate.

In TRA, as seen in Fig. 18(a), the transient vertical displacement at the upper surface of phononic crystal plate is shown when the time ranges from 0 to 200 μs. Transforming the vertical displacement from time domain to frequency domain and normalizing by the transmitted power spectrum of homogeneous plate, we can obtain the normalized transmitted power spectrum of phononic crystal plate with periodic superlattice, as shown

in Fig. 18(b), and an obvious band gap is observed in the range from 0.9512 to 1.047 MHz, which means the elastic wave located in this gap is extremely attenuated. Applying the Super-cell PWE or HRA, we recalculate the band structure and normalized transmitted power spectrum, respectively for comparison and the data are shown in Fig. 19.

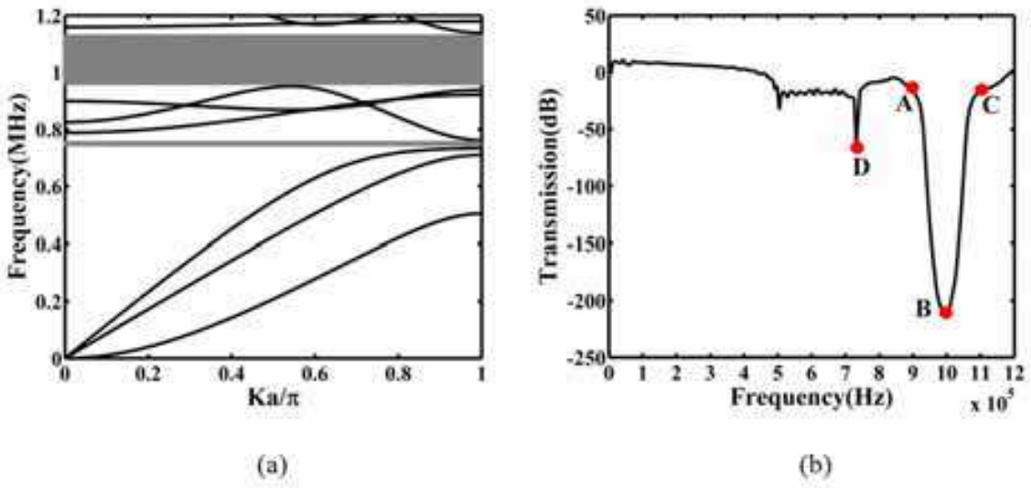

Fig. 19. (a) Dispersion curves of Lamb wave modes for phononic crystal plate without substrate, calculated by Super-cell PWE; (b) Normalized transmitted power spectrum for phononic crystal plate without substrate, calculated by HRA method.

From both Fig. 19(a) and 19(b), we can see a main band gap located around 1 MHz (0.9511~1.1300 MHz in Fig. 19(a); 0.9510~1.0560 MHz in Fig. 19(b)), which accords with the Fig. 18(b). Note that there exists a very narrow band gap in low frequency zone as shown in Fig. 19(a) (0.7332 MHz~0.762 MHz), or the D point (0.7335 MHz) in Fig. 19(b). Therefore, the result of HRA is more consistent with Super-cell PWE than of TRA, and importantly the HRA method is more efficient in calculations of not only normalized transmitted power spectrum but also space distribution of elastic wave field for the reason mentioned above. Hereon we choose three points (A: 0.9 MHz, B: 1 MHz, C: 1.1 MHz) in Fig. 19(b) for the study of propagation of Lamb waves under different frequency loads (inside/outside the band gap).

As seen from Fig. 20, the displacement fields under different frequency loads are quite different. In Fig. 20(b), the load frequency locates inside the band gap and the displacement field seems like being blocked by the superlattice, in which the periodic structure forbids the propagation of elastic waves along the plate. However, when the load frequency locates outside the band gap in Fig. 20(a) and 20(c), the elastic waves propagate without any obvious attenuation.

Then, we add an extra substrate to the established model. The thickness of substrate is set to be 0.2 mm. Applying the Super-cell PWE and HRA, we can obtain the dispersion curves of Lamb wave modes and normalized transmitted power spectrum, respectively, as shown in Fig. 21, in which the first band gap exists in low frequency zone (0.7413~0.7767 MHz in Fig. 21(a); 0.7520~0.7730 MHz in Fig. 21(b)) and the main band gap (second band gap) locates at high frequency zone (0.9852~1.1240 MHz in Fig. 21(a); 0.9853~1.0580 MHz in Fig. 21(b)). Comparing Fig. 21 with Fig. 19, one can observe that the first band gap width in the plate with substrate is larger than that of the plate without substrate and main band gap (the

second band gap) width is narrowed and shifted towards high frequency zone, which accord with previous works [4,23,42].

In addition to the periodic systems, we adopt the HRA to study the quasiperiodic systems. The normalized transmitted power spectra are calculated for phononic crystal plates with the above three quasiperiodic systems, as shown in Fig. 22(a)-(c), in which the normalized transmitted power spectrum of periodic system is also plotted for comparison.

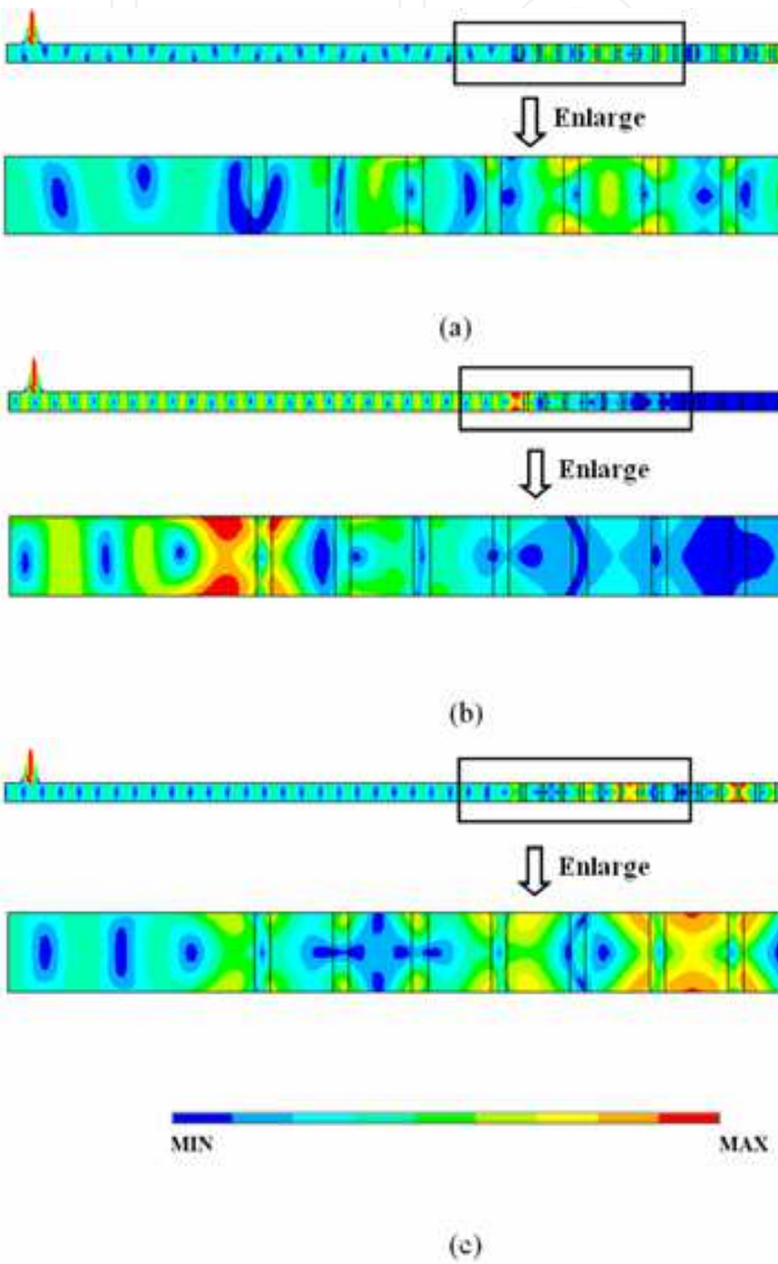

Fig. 20. The displacement fields at the frequency loads of 0.9 MHz (A point in Fig. 19(b)) (a), 1 MHz (B point in Fig. 19(b)) (b) and 1.1 MHz (C point in Fig. 19(b)) (c), respectively. Corresponding plot in each figure is enlarged.

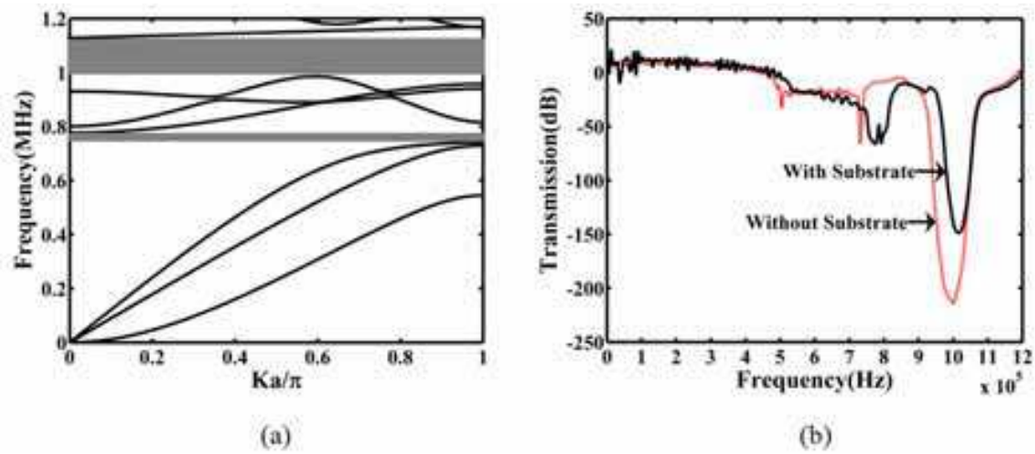

Fig. 21. (a) Dispersion curves of Lamb wave modes for phononic crystal plate with substrate, calculated by Super-cell PWE; (b) Normalized transmitted power spectra for phononic crystal plates both with and without substrate (substrate thickness: 0.2 mm), calculated by HRA method.

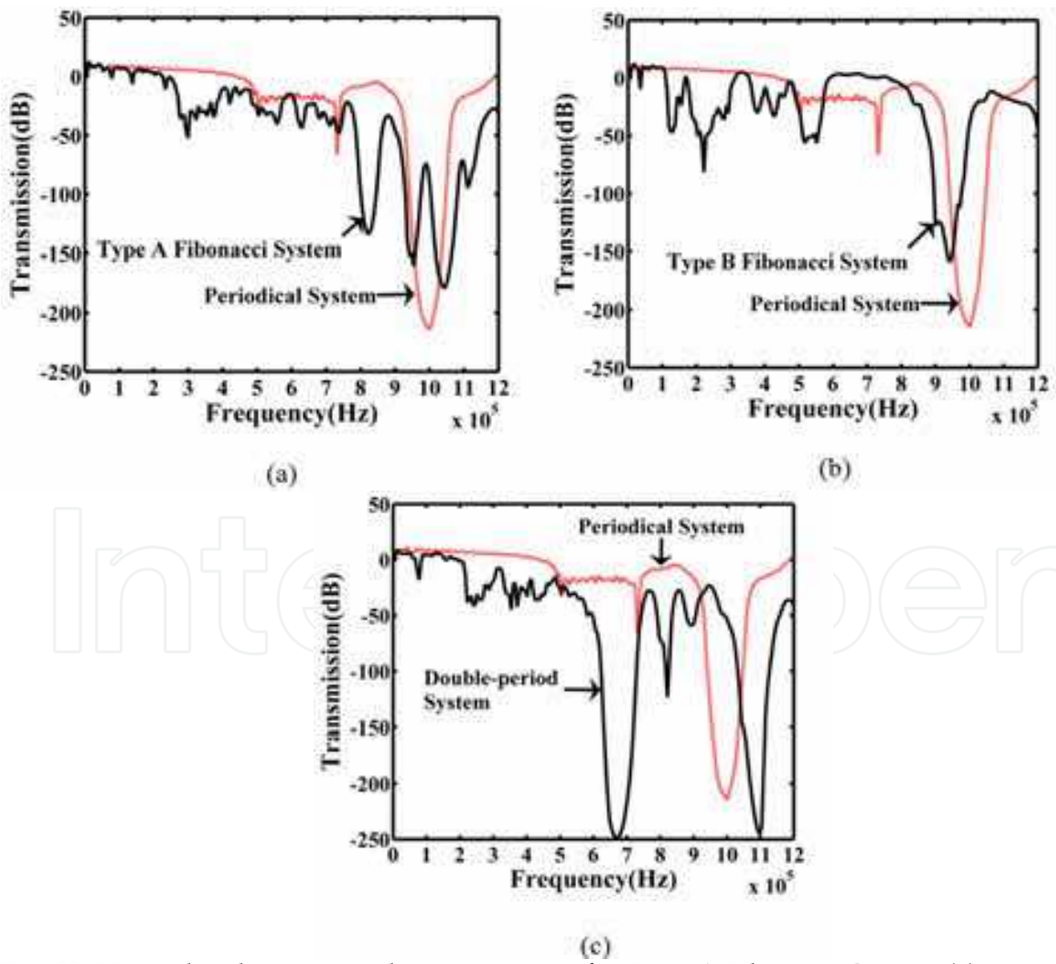

Fig. 22. Normalized transmitted power spectra for Type A Fibonacci System (a), Type B Fibonacci System (b) and Double-period System (c), respectively.

As shown in Fig. 22(a), for Type A Fibonacci System, a new band gap is opened in low frequency zone (0.7925~0.8622 MHz) and the main band gap (corresponding to the one in the periodic system) splits into two separated sub-band gaps (0.9282~0.9667 MHz and 0.9942~1.0730 MHz). In addition, an obvious attenuation is observed in lower frequency zone (0.276~0.384 MHz).

For Type B Fibonacci System, the main band gap shifts to the low frequency zone (0.8915~0.9978 MHz) with its gap width almost unchanged, as shown in Fig. 22(b), and three new band gaps form in lower frequency zone (0.114~0.162 MHz, 0.192~0.288 MHz and 0.498~0.57 MHz).

For Double-period System, the main band gap shifts to high frequency zone (1.0180~1.1340 MHz) and four new band gaps are opened in the low frequency zone (0.216~0.294 MHz, 0.336~0.468 MHz, 0.6238~0.7265 MHz and 0.792~0.84 MHz), as shown in Fig. 22(c).

From the above-mentioned information, we convincingly demonstrate the band gap distribution of quasiperiodic systems is more complicated and meaningful than of periodic systems and the reason is supposed to be that quasiperiodicity unlike periodicity can provide more than one reciprocal lattices.

6. Band gaps of plate-mode waves in 1D piezoelectric composite plates without/with substrates

As well known, the ceramic material will have the piezoelectricity only after it is polarized. In convenience, we define the non-polarized PZT-5H ceramic as the non-piezoelectric material, which has the same elastic constants as the polarized PZT-5H. Fig. 23 provides five schematic representations of the plate-mode waves for non-polarization, *x*-polarization with OC, *x*-polarization with SC, *z*-polarization with OC, and *z*-polarization with SC, respectively. The first band gaps (FBG) widths shown by the gray area in Fig. 23(a)-(e) are 2.088, 2.072, 2.368, 2.368, and 2.6 MHz, respectively. On the whole, the FBG are always broadened by polarizing piezoelectric ceramics at the same values of f and h/D. Comparing the Fig. 23(b) and (c) (or Fig. 23(d) and (e)), the FBG width with SC is larger than that with OC for the same polarized direction, whereas the FBG width of *z*-polarization with SC is the largest. In our example, the FBG width of *z*-polarization with OC is equal to the FBG width of *x*-polarization with SC, which means the *z*-polarized PZT-5H ceramics is easy to produce a larger FBG width.

The V-PWE method is applied to calculate the dispersion curves of Lamb wave propagating in the *x*-direction when the existence of uniform substrate. Since the substrate affects the width and starting frequency of the PC layer, the thickness of the substrate will be an important parameter of the system. Meanwhile, the filling fraction f is another critical parameter that affects the formation, width and starting frequency of the FBG [43,44]. Fig. 24 (a) and (b) display the dependence of the FBG widths and starting frequencies with the filling fraction f and the ratio of h_2 to h_1 at h_1 =0.8mm, D =2mm with OC when the PC layer is coated on an epoxy substrate. As shown in Fig. 24(a), the FBG width increases progressively with the increase of the value of f at a certain value of h_2 / h_1 until a critical value then decreases and the width decreases gradually with the increase of the value of h_2 / h_1 at a certain value of f. The FBG width takes the maximum value when there is no substrate, and decreases with the increase of the substrate's thickness at any values of f. The FBG width takes a larger value when f and h_2 / h_1 take values in the domain 0.45-0.65

and 0-0.8, respectively. This domain is useful in the engineering field. The FBG width decreases slowly when h_2 / h_1 takes values from 0 to 0.4 (Δh_{slow}) and decreases rapidly when h_2 / h_1 takes values from 0.4 to 0.80 (Δh_{rapid}) as f takes values from 0.45 to 0.65(Δf). As shown in Fig. 25(b), the FBG starting frequency decreases gradually with the increase of the value of f at a certain value of h_2 / h_1 until a critical value then increases. The starting frequency increases progressively with the increase of the value of h_2 / h_1 at a certain value of f until a critical value then decreases, but the change of the starting frequency is small. On the whole, the epoxy substrate reduces the FBG width obviously and has little influence on the FBG starting frequency.

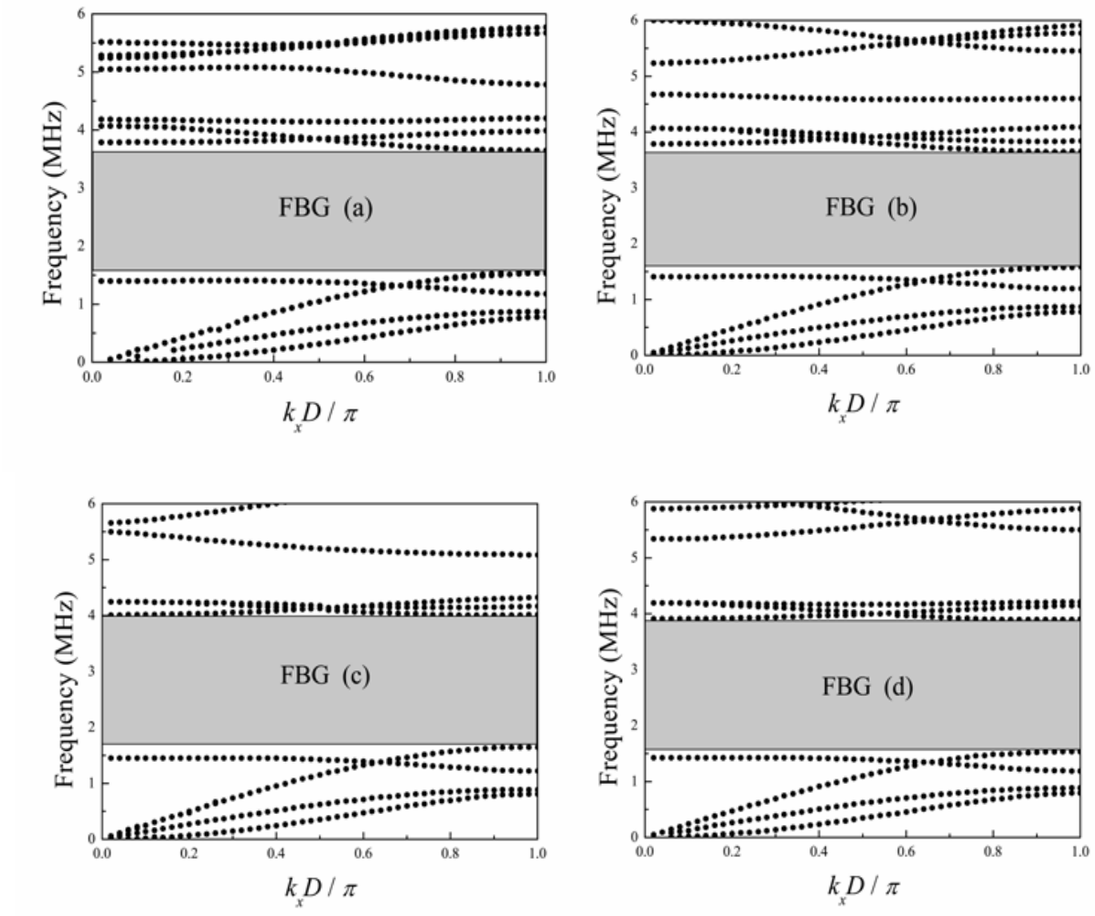

Fig. 23. The 1D plate-mode waves for different polarizations under different boundary conditions with $f = 0.5$ and h / D =0.8 (D=2mm): (a) Non-polarization, (b) x-polarization with OC, (c) x-polarization with SC, (d) z-polarization with OC, and (e) z-polarization with SC.

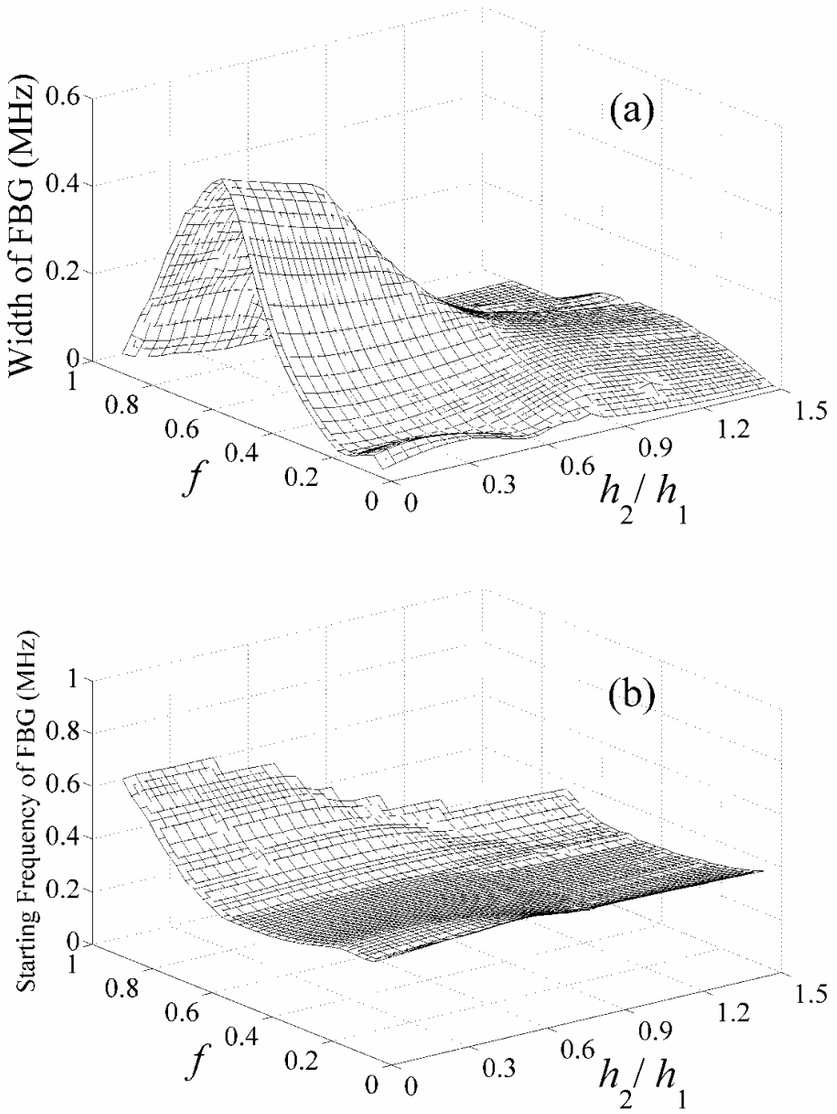

Fig. 24. The FBG widths (a) and starting frequencies (b) versus f and h_2 / h_1 (h_1 =0.8mm, D =2mm) with OC coated on epoxy substrate.

7. Conclusions

In this chapter, we first examine the band structures of lower-order Lamb wave modes propagating in the 1D periodic composite thin plate based on the PWE for infinitely long periodic systems and have calculated the TPS for finite systems by using the FE method. As shown, the TPS through a superlattice with ten periods has prominent dips at frequencies corresponding to the gaps in band structure. A crucial parameter, namely, the ratio of L/D, was discussed, and the value of the ratio of L/D was emerging as critical parameters in determining the existence of band gaps for the Lamb waves in the periodic structures. Thus, we can achieve the needed width of band gap for Lamb wave by varying the thickness of

plate. Then, we study the substrate effect on the band gaps of lower-order Lamb waves propagating in thin plate with 1D phononic crystal layer coated on uniform substrate. The results show that when the substrate is hard, the influences on band gap are significant, and the band gaps disappear rapidly as the substrate becomes thicker. However, when the substrate is soft, the depth of band gaps becomes larger as the thickness of substrate increases. A virtual plane wave expansion method is developed to calculate the dispersion curves of Lamb wave. The locations and widths of band gaps on the dispersion curves are in good agreement with the results from the transmitted power spectra by FEM.

The band gap structure of Lamb waves in the 1D quasiperiodic composite thin plate is also studied by calculating the TPS from the FEM. The band gap structures of the Lamb waves are quite different from those of bulk waves. Specifically, the number of splitting band gaps depends strongly on the values of L/D owing to resonance of the coupling of the longitudinal and transversal strain components at the plate boundaries. However, the split of band gaps is independent of the layer number of Fibonacci sequences. Moreover, we have found that the structure of the band gaps depends very sensitively on the thickness ratio of the sublattices A and B in the quasiperiodic structures which might find applications in nondestructive diagnosis.

We have promoted an efficient HRA method to investigate the acoustic wave behavior in silicon-based 1D phononic crystal plates. The HRA method can not only save much time in the calculation of transmitted power spectrum but also acquire information of the displacement field under different frequency loads at the same time. Applying HRA and supercell PWE, we have studied the periodic structures both without and with substrate. From the displacement field map, we find that the elastic wave is completely blocked by the superlattice when the load frequency is inside the acoustic band gap. After introducing different kinds of quasiperiodic structures, we studied the normalized transmitted power spectra in details and find out that the original main band gap in periodic structure may split or shift to low or high frequency zones in different quasiperiodic structures. Furthermore, new band gaps in low frequency zone may be opened which provide potential application in the field of wave filtering as well as sound isolation.

Finally, we study the band gaps of plate-mode waves in 1D piezoelectric composite plates without/with substrates. We found that the FBG is always broadened by polarizing piezoelectric ceramics, and the FBG widths with SC are always larger than that with OC for the same polarization. The FBG width decreases gradually as the substrate's thickness increases and the FBG starting frequency increases progressively as the thickness increases on the whole. Our researches show that it is possible to control the width and starting frequency of the FBG in the engineering according to need by choosing suitable values of the substrate's thickness, the filling fraction with different electrical boundary conditions.

8. References

[1] J. J. Chen, K. W. Zhang, J. Gao, and J. C. Cheng, Phys. Rev. B 73, 094307 (2006).
[2] J. Gao, J. C. Cheng, and B. W. Li, Appl. Phys. Lett. 90, 111908 (2007).
[3] J. H. Sun and T. T. Wu, Phys. Rev. B 74, 174305 (2006).
[4] J. O. Vasseur, P. A. Deymier, B. Djafari-Rouhani, Y. Pennec, and A. -C. Hladky-Hennion, Phys. Rev. B 77, 085415 (2008).

[5] S. Mohammadi, A. A. Eftekhar, A. Khelif, W. D. Hunt, and A. Adibi, Appl. Phys. Lett. 92, 221905 (2008).
[6] S. Mohammadi, A. A. Eftekhar, W. D. Hunt, and A. Adibi, Appl. Phys. Lett. 94, 051906 (2009).
[7] C. J. Rupp, M. L. Dunn, and K. Maute, Appl. Phys. Lett. 96, 111902 (2010).
[8] J. Gao, X. Y. Zou, and J. C. Cheng, Appl. Phys. Lett. 92, 023510 (2008).
[9] X. F. Zhu, T. Xu, S. C. Liu, and J. C. Cheng, J. Appl. Phys. 106, 104901 (2009).
[10] X.-Y. Zou, B. Liang, Q. Chen, and J.-C. Cheng, IEEE Trans. Ultrason. Ferroelectr. Freq. Control 56, 361 (2009).
[11] B. A. Auld, Y. A. Shui, and Y. Wang, J. Phys. (Paris) 45, 159 (1984).
[12] B. A. Auld and Y. Wang, Proc.-IEEE Ultrason. Symp. 528 (1984).
[13] A. Alippi, F. Craciun, and E. Molinari, Appl. Phys. Lett. 53, 1806 (1988).
[14] A. Alippi, F. Craciun, and E. Molinari, J. Appl. Phys. 66, 2828 (1989).
[15] S. G. Joshi and Y. Jin, J. Appl. Phys. 69, 8018 (1991).
[16] M. Wilm, S. Ballandras, V. Laude, and T. Pastureaud, J. Acoust. Soc. Am. 112, 943 (2002).
[17] S. Zhang and J. C. Cheng, Phys. Rev. B 68, 245101 (2003).
[18] F. Moser, L. J. Jacobs, and J. M. Qu, NDT & E Int. 32, 225 (1999).
[19] K. J. Bathe, Finite Element Procedures, Prentice-Hall, Englewood Cliffs, NJ, 1996.
[20] Y. Gu, J. Liu and Y. Du, Engineering Mechanics 24, 12 (2007) (Chinese).
[21] X. F. Zhu, S. C. Liu, T. Xu, T. H. Wang, and J. C. Cheng, Chin. Phys. B 19, 4 (2010).
[22] Y. Tanaka, Y. Tomoyasu, and S. I. Tamura, Phys. Rev. B 62, 7387 (2000).
[23] Z. L. Hou and B. M. Assouar, Phys. Lett. A 372, 2091 (2008).
[24] Y. Zhang and H. Zhao, Phys. Rev. E 66, 026106 (2002).
[25] J. C. Cheng, S. Y. Zhang, and L. Wu, Appl. Phys. A: Mater. Sci. Process. 61, 311 (1995).
[26] Y. J. Cao and Y. Xu, Actra Physica Sinica 57, 3620 (2008).
[27] E. L. Albuquerque and M. G. Cottam, Physics Reports 376, 225 (2003).
[28] W. A. Smith and B. A. Auld, IEEE Trans. Ultrason. Ferroelectr. Freq. Control 38, 40 (1991).
[29] M. S. Kushwaha, Appl. Phys. Lett. 70, 3218 (1997).
[30] J. C. Cheng and S. Y. Zhang, Appl. Phys. Lett. 74, 2087 (1999).
[31] S. Linden, J. Kuhl, and H. Giessen, Phys. Rev. Lett. 86, 4688 (2001).
[32] S. Ostlund, R. Pandit, D. Rand, H. J. Schellnhuber, and E. D. Siggia, Phys. Rev. Lett. 50, 1873 (1983).
[33] D. Shechtman, I. Blech, D. Gratias, and J. W. Cahn, Phys. Rev. Lett. 53, 1951 (1984).
[34] R. Merlin, K. Bajema, R. Clarke, F. -Y. Juang, and P. K. Bhattacharya, Phys. Rev. Lett. 55, 1768 (1985).
[35] J. Todd, R. Merlin, R. Clarke, K. M. Mohanty, and J. D. Axe, Phys. Rev. Lett. 57, 1157 (1986).
[36] C. Wang and R. A. Barrio, Phys. Rev. Lett. 61, 191 (1988).
[37] J. -P. Desideri, L. Macon, and D. Sornette, Phys. Rev. Lett. 63, 390 (1989).
[38] M. W. C. Dharma-Wardana, A. H. MacDonald, D. J. Lockwood, J. -M. Baribeau, and D. C. Houghton, Phys. Rev. Lett. 58, 17 (1987).
[39] S. Tamura and J. P. Wolfe, Phys. Rev. B 36, 6 (1987).
[40] Y. E. Hassouani, H. Aynaou, E. H. E. Boudouti, B. Djafari-Rouhani, A. Akjouj, and V. R. Velasco, Phys. Rev. B 74, 035314 (1990).
[41] J. Q. You, Q. B. Yang, and J. R. Yan, Phys. Rev. B 41, 11 (1990).
[42] Z. Hou and B. M. Assouar, J. Phys. D: Appl. Phys. 42, 0850103 (2009).
[43] X.-Y. Zou, Q. Chen, B. Liang, and J.-C. Cheng, Smart Mater. Struct. 17, 015008 (2008)
[44] X.-Y. Zou, Q. Chen, and J.-C. Cheng, IEEE Trans. Ultrason. Ferroelectr. Freq. Control 54, 1430 (2007).

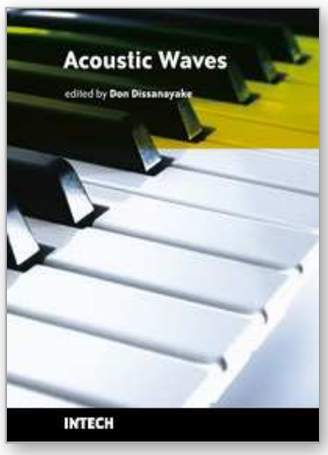

Acoustic Waves
Edited by Don Dissanayake

ISBN 978-953-307-111-4
Hard cover, 434 pages
Publisher Sciyo
Published online 28, September, 2010
Published in print edition September, 2010

SAW devices are widely used in multitude of device concepts mainly in MEMS and communication electronics. As such, SAW based micro sensors, actuators and communication electronic devices are well known applications of SAW technology. For example, SAW based passive micro sensors are capable of measuring physical properties such as temperature, pressure, variation in chemical properties, and SAW based communication devices perform a range of signal processing functions, such as delay lines, filters, resonators, pulse compressors, and convolvers. In recent decades, SAW based low-powered actuators and microfluidic devices have significantly added a new dimension to SAW technology. This book consists of 20 exciting chapters composed by researchers and engineers active in the field of SAW technology, biomedical and other related engineering disciplines. The topics range from basic SAW theory, materials and phenomena to advanced applications such as sensors actuators, and communication systems. As such, in addition to theoretical analysis and numerical modelling such as Finite Element Modelling (FEM) and Finite Difference Methods (FDM) of SAW devices, SAW based actuators and micro motors, and SAW based micro sensors are some of the exciting applications presented in this book. This collection of up-to-date information and research outcomes on SAW technology will be of great interest, not only to all those working in SAW based technology, but also to many more who stand to benefit from an insight into the rich opportunities that this technology has to offer, especially to develop advanced, low-powered biomedical implants and passive communication devices.

InTech Europe
University Campus STeP Ri
Slavka Krautzeka 83/A
51000 Rijeka, Croatia
Phone: +385 (51) 770 447

InTech China
Unit 405, Office Block, Hotel Equatorial Shanghai
No.65, Yan An Road (West), Shanghai, 200040, China
中国上海市延安西路65号上海国际贵都大饭店办公楼405单元
Phone: +86-21-62489820

Fax: +385 (51) 686 166
www.intechopen.com

Fax: +86-21-62489821

IntechOpen

IntechOpen